Published online 15 February 2022

Nucleic Acids Research, 2022, Vol. 50, No. 4 ***1829–1848***
https://doi.org/10.1093/nar/gkac090

Rational design of small-molecules to recognize G-quadruplexes of c-MYC promoter and telomere and the evaluation of their *in vivo* antitumor activity against breast cancer

Wei Long[1], Bo-Xin Zheng[1], Ying Li[1], Xuan-He Huang[1], Dan-Min Lin[1], Cui-Cui Chen[1], Jin-Qiang Hou[4,5], Tian-Miao Ou[6], Wing-Leung Wong[2,*], Kun Zhang[1,3,*] and Yu-Jing Lu[1,*]

[1]School of Biomedical and Pharmaceutical Sciences, Guangdong University of Technology, Guangzhou 510006, PR China, [2]State Key Laboratory of Chemical Biology and Drug Discovery, Department of Applied Biology and Chemical Technology, The Hong Kong Polytechnic University, Hung Hom, Hong Kong SAR, China, [3]School of Biotechnology and Health Sciences, Wuyi University, Jiangmen, 529020, P.R. China; International Healthcare Innovation Institute (Jiangmen), Jiangmen, 529040, PR China, [4]Department of Chemistry, Lakehead University, 955 Oliver Road, Thunder Bay, Ontario P7B 5E1, Canada, [5]Thunder Bay Regional Health Research Institute, 980 Oliver Road, Thunder Bay, Ontario P7B 6V4, Canada and [6]Guangdong Provincial Key Laboratory of New Drug Design and Evaluation, School of Pharmaceutical Sciences, Sun Yat-Sen University, Guangzhou 510006, China

Received July 21, 2021; Revised January 20, 2022; Editorial Decision January 24, 2022; Accepted January 27, 2022

ABSTRACT

DNA G4-structures from human c-MYC promoter and telomere are considered as important drug targets; however, the developing of small-molecule-based fluorescent binding ligands that are highly selective in targeting these G4-structures over other types of nucleic acids is challenging. We herein report a new approach of designing small molecules based on a non-selective thiazole orange scaffold to provide two-directional and multi-site interactions with flanking residues and loops of the G4-motif for better selectivity. The ligands are designed to establish multi-site interactions in the G4-binding pocket. This structural feature may render the molecules higher selectivity toward c-MYC G4s than other structures. The ligand–G4 interaction studied with ^{1}H NMR may suggest a stacking interaction with the terminal G-tetrad. Moreover, the intracellular co-localization study with BG4 and cellular competition experiments with BRACO-19 may suggest that the binding targets of the ligands in cells are most probably G4-structures. Furthermore, the ligands that either preferentially bind to c-MYC promoter or telomeric G4s are able to downregulate markedly the c-MYC and hTERT gene expression in MCF-7 cells, and induce senescence and DNA damage to cancer cells. The *in vivo* antitumor activity of the ligands in MCF-7 tumor-bearing mice is also demonstrated.

GRAPHICAL ABSTRACT

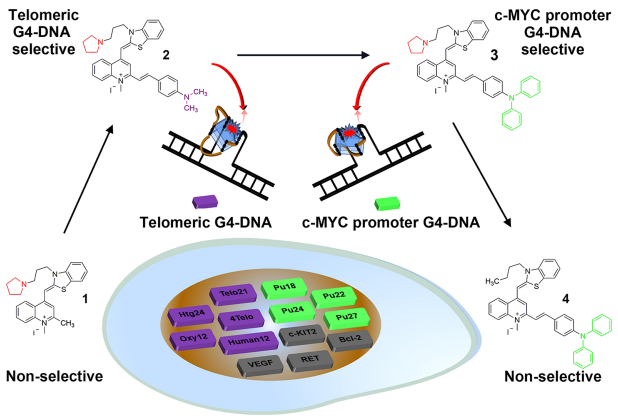

INTRODUCTION

Nucleic acids such as deoxyribonucleic acid (DNA) and ribonucleic acid (RNA) are important genetic substances that play many vital roles in life activities (1,2). The structure of nucleic acids is complicated due to the formation

*To whom correspondence should be addressed. Tel: +852 34008871; Fax: +852 23649932; Email: wing.leung.wong@polyu.edu.hk
Correspondence may also be addressed to Kun Zhang. Tel: +86 13602890906; Email: kzhang@gdut.edu.cn
Correspondence may also be addressed to Yu-Jing Lu. Tel: +86 15521451995; Email: luyj@gdut.edu.cn

© The Author(s) 2022. Published by Oxford University Press on behalf of Nucleic Acids Research.
This is an Open Access article distributed under the terms of the Creative Commons Attribution-NonCommercial License (http://creativecommons.org/licenses/by-nc/4.0/), which permits non-commercial re-use, distribution, and reproduction in any medium, provided the original work is properly cited. For commercial re-use, please contact journals.permissions@oup.com

Downloaded from https://academic.oup.com/nar/article/50/4/1829/6528910 by guest on 04 March 2022

of various higher-order structures through interactions between bases under different conditions. These structures are generally believed to have certain unique functionality that regulates cellular activities but most biological mechanisms related to the higher-order structures are not fully understood. The study of higher-order structures of DNA and RNA is thus a significant research topic, particularly in quantitative analysis, specific identification, genomics development, and functional gene research and applications (3–6). The real-time identification of any specific types of DNA structures such as G-quadruplexes (G4) *in vivo* to monitor their structural dynamics and to investigate their biological activity in live cell is a challenging task (7–9).

The number of possible G4–DNA motifs in the human genome could reach 700,000 or more (10). It is important to establish a highly selective molecular tool for the discrimination of the G4–DNA structures in cells so that the probing of the existence of certain G4–DNA structures under certain conditions in live cells or *in vivo*, and the understanding of the associated biofunctions could be achieved (11). However, it is complicated to predict and recognize all these unique molecules in high specificity because the G4-structures mostly share the same core structure of guanine-tetrads despite their loops and flanking sequences at both 3′- and 5′-terminal are significantly different (12,13). Ligands that are designed with functional groups that target the loops and/or flanking sequences and the guanine-tetrad may achieve better interaction with or discrimination of G4-structures over other types of nucleic acids. In recent years, G4-structures have been a hot research topic in the discovery of *in vivo* functions in regulating telomere maintenance, transcription, replication, and translation (14). Many of these G4-structures are found to be evolutionary conserved (15). The molecular recognition and stabilization of G4-structures formed in c-MYC promoter and telomere are considered as an important strategy for the fundamental study of G4 biofunctions and novel anticancer drug design (16). There is accumulating evidence demonstrating that G4-structures of c-MYC promoter, such as Pu27, are a very vital target for cancer research. Some recent studies have identified that the expression of c-MYC oncogene is closely linked to the potentiation of cellular proliferation and inhibition of cell differentiation (17–19). About 20% of human tumors are found to be associated with c-MYC overexpression (20). A few lately reported molecular binders that stabilize the c-MYC promoter G4–DNA are found to be able to inhibit tumor growth *in vivo* (21–24), which supports that c-MYC could be an important drug target. The nuclease hypersensitivity element III_1 (NHE III_1) is a 27-bp sequence (Pu27) located −142 to −115 bp upstream from the P1 promoter of c-MYC, and it controls 85–90% of c-MYC transcription (25). The DNA sequence of Pu27 is guanine rich and is able to form thermodynamically stable G4-structures. It has been reported that a cationic porphyrin ($TMPyP_4$) that stabilizes the G4-structure of Pu27 is able to lower c-MYC transcription and protein expression, and suppress the transcriptional activation of downstream genes that are involved in proliferation of cancer cells, such as hTERT, ODC and CDC25A (25,26). These biological effects could be interrupted through the interaction of G4-ligands with the G4-structure of Pu27 and thus the helicase-mediated unwinding of G4-structures is inhibited (25).

A variety of effective G4-binding ligands that target telomeric G4–DNA has been reported in the past few decades (27–30). On the other hand, reports on ligands that target c-MYC G4s for fluorescent recognition, sensing, and stabilization of G4-structures in live cell or *in vivo* are relatively rare, which may imply current understanding on the designing of c-MYC G4-selective ligands for molecular recognition and fundamental study of G4s in cells or *in vivo* is still limited (31–35). Although a few probes that show high selectivity in the recognition of the c-MYC G4 via the fluorescent visualization approach have been reported (36–39), the mechanism underlying the structural discrimination is still unclear. We herein report a rational design of small molecule-based ligands for the recognition and visualization of c-MYC G4–DNA structures in solution and in cells *via* a fluorescence light-up mechanism. In the present study, we systematically demonstrated how each substituent group integrated in the thiazole orange scaffold taking effects in controlling the G4-structure selectivity in terms of the fluorescent signal induced from ligand–G4 interactions. The ligands that possessed a two-directional and multi-site interaction system were found to be able to achieve highly selective toward c-MYC G4s. The possible interaction modes of the ligands with c-MYC G4–DNA were studied with ^{1}H NMR and molecular modeling. In addition, the intracellular co-localization study with BG4 demonstrated that the ligands were selective to G4-structures. These new G4-ligands also showed good cytotoxicity against a panel of human cancer cells and exhibited potent *in vivo* antitumor activity against MCF-7 breast cancer.

MATERIALS AND METHODS

Instruments

High-resolution mass spectra (HRMS) were obtained by Agilent 1260–6230TOF. Using TMS as a reference, ^{1}H and ^{13}C NMR spectra were recorded at 400 MHz and 100 MHz in DMSO-d_6 with a Bruker BioSpin GmbH spectrometer. The high performance liquid chromatography (HPLC) analysis for examining the purity of the compounds was performed on an SHIMADZU LC-16 system using a Diamonsil C18 column (250 × 4.6 mm, 5 μm) at room temperature with an elution using the mobile phase ($MeOH/H_2O$ = 50:50 v/v). Unless otherwise stated, all chemicals were purchased from commercial sources. All solvents were analytical reagent grade and could be used without further purification. All oligonucleotides used in this work were synthesized and purified by Shanghai Sangon Biotechnology Co., Ltd. (Shanghai, China). Upon receipt, the oligonucleotides were dissolved in Tris–HCl buffer (10 mM, pH 7.4, containing 60 mM KCl or without ion) and stored at −20°C until use. Folding was achieved by diluting the oligonucleotides into their respective buffers and heating in a water bath to 95°C for 20 min, then slowly cooled overnight and stored at 4°C. Their sequences were listed in Supplementary Table S1 and the structures were characterized with circular dichroism (CD) spectroscopy with respect to literature (40–42).

Downloaded from https://academic.oup.com/nar/article/50/4/1829/6528910 by guest on 04 March 2022

General procedures for the synthesis of compounds 1–4

Compound **1** was obtained by the reaction using a bromopropyl substituted thiazole orange (1,2-dimethyl-4-[(3-bromopropyl-2(3H)-benzothiazolylidene)methyl]quinolinium iodide, 1.103 g, 2.0 mmol) and pyrrolidine (0.8 mL), potassium iodide (0.332 g, 2.0 mmol) in 40°C for 24 h. Further reaction of **1** (1.103 g, 2.0 mmol) with an aromatic aldehyde including 4-(diphenylamino)benzaldehyde (1.092 g, 4.0 mmol) or 4-(dimethylamino)benzaldehyde (0.596 g, 4.0 mmol) and 4-methylpiperidine (200 μl) in n-butanol (10 mL) was conducted under reflux conditions (about 135°C) for 3 h to afford target compound **2** and **3** in good yields. For the synthesis of compound **4**, an intermediate was prepared by the reaction using 4-chloro-1,2-dimethylquinolin-1-ium (0.638 g, 2.0 mmol) and 3-butyl-2-methylbenzo[d]thiazol-3-ium bromide (0.572 g, 2.0 mmol) in 40°C for 3 h. After that, the reaction was further reacted with 4-(diphenylamino)benzaldehyde (1.092 g, 4.0 mmol) and 4-methylpiperidine (200 μl), n-butanol (10 mL), potassium iodide (0.332 g, 2.0 mmol) in 135°C refluxed for 3 h to afford **4** in good yields. (Supplementary Figure S1) All these compounds were purified by flash silica gel column chromatography and were confirmed with ^{1}H NMR, ^{13}C NMR, HRMS and HPLC. The purity of all these compounds determined by HPLC is higher than 95%. (Supplementary Figure S26–S29)

Compound **1** (43): 92.6% yield. ^{1}H NMR (400 MHz, DMSO-d_6) δ 8.62 (d, J = 8.4 Hz, 1H), 8.15 (d, J = 8.4 Hz, 1H), 7.98 (m, 2H), 7.72 (m, 2H), 7.56 (t, J = 7.6 Hz, 1H), 7.37 (t, J = 7.6 Hz, 1H), 7.29 (s, 1H), 6.94 (s, 1H), 4.61 (t, J = 6.5 Hz, 2H), 4.05 (s, 3H), 2.86 (s, 3H), 2.46 (m, 2H), 2.36 (m, 4H), 2.01–1.94 (m, 2H), 1.63 (m, 4H). ^{13}C NMR (101 MHz, DMSO-d_6) δ 159.28, 154.54, 148.33, 140.62, 139.51, 133.55, 128.47, 126.72, 125.50, 124.69, 124.29, 123.90, 123.21, 118.83, 113.24, 110.97, 100.00, 87.08, 53.89, 52.45, 44.18, 37.63, 26.45, 23.63, 23.35. HRMS m/z: calcd for $C_{26}H_{30}N_3S^+$ [M-I]$^+$ 416.2155; found 416.2158 [M-I]$^+$. HPLC analysis: retention time at 3.212 min eluted with MeOH/H_2O = 50:50 (v/v), purity = 96%.

Compound **2**: 88.7% yield. ^{1}H NMR (400 MHz, DMSO-d_6) δ 8.58 (d, J = 8.4 Hz, 1H), 8.16 (d, J = 8.4 Hz, 1H), 8.05 (d, J = 7.6 Hz, 1H), 7.96 (t, J = 7.6 Hz, 1H), 7.80 (d, J = 8.8 Hz, 2H), 7.69 (m, 4H), 7.59 (t, J = 7.6 Hz, 1H), 7.47 (d, J = 7.6 Hz, 1H), 7.37 (t, J = 7.6 Hz, 1H), 6.96 (s, 1H), 6.81 (d, J = 8.8 Hz, 2H), 4.61 (t, J = 6.4 Hz, 2H), 4.15 (s, 3H), 3.05 (s, 6H), 2.49–2.32 (m, 4H), 1.99 (s, 2H), 1.78–1.62 (m, 4H), 1.18 (t, J = 6.4 Hz, 2H). ^{13}C NMR (101 MHz, DMSO) δ 158.40, 153.16, 152.30, 140.74, 139.60, 130.96, 126.52, 125.19, 124.25, 123.39, 123.14, 119.00, 115.11, 112.82, 112.17, 108.05, 87.24, 53.93, 52.46, 38.29, 23.63. HRMS m/z: calcd for $C_{35}H_{39}N_4S^+$ [M−I]$^+$ 547.2890; found 547.2937 [M−I]$^+$. HPLC analysis: retention time at 2.777 min eluted with MeOH/H_2O = 50:50 (v/v), purity = 98%.

Compound **3**: 86.1% yield. ^{1}H NMR (400 MHz, DMSO-d_6) δ 8.58 (d, J = 8.4 Hz, 1H), 8.14 (d, J = 8.8 Hz, 1H), 8.03 (d, J = 7.6 Hz, 1H), 7.97 (t, J = 7.6 Hz, 1H),7.81 (d, J = 8.8 Hz, 2H), 7.71 (d, J = 8.0 Hz, 2H), 7.63–7.54 (m, 4H), 7.43–7.36 (m, 5H), 7.17 (t, J = 7.6 Hz, 2H), 7.12 (d, J = 7.6 Hz, 4H), 7.00 (d, J = 8.8 Hz, 3H), 4.62 (t, J = 6.4 Hz, 2H), 4.12 (s, 3H), 2.50–2.47 (m, 2H), 2.39 (s, 4H), 2.05–1.95 (m, 2H), 1.67 (s, 4H). ^{13}C NMR (101 MHz, DMSO-d_6) δ 159.22, 152.69, 149.75, 147.94, 146.84, 141.12, 140.70, 139.57, 133.61, 130.37, 128.94, 128.49, 125.54, 125.27, 124.69, 124.34, 123.99, 121.69, 119.42, 119.07, 108.39, 87.79, 53.93, 52.49, 44.20, 38.44, 26.52, 23.67. HRMS m/z: calcd for $C_{45}H_{43}N_4S^+$ [M−I]$^+$ 671.3203; found 671.3237 [M−I]$^+$. HPLC analysis: retention time at 2.789 min eluted with MeOH/H_2O = 50:50 (v/v), purity >99.5%.

Compound **4**: 81.4% yield. ^{1}H NMR (400 MHz, DMSO-d_6) δ 8.71 (s, 1H), 8.17 (s, 1H), 8.01 (d, J = 8.6 Hz, 2H), 7.91–7.69 (m, 4H), 7.67–7.53 (m, 3H), 7.41 (t, J = 6.5 Hz, 3H), 7.15 (m, 5H), 7.00 (m, 2H), 6.89 (s, 2H), 6.71 (s,2H), 4.57 (s, 2H), 4.15 (s, 3H), 1.84 (s, 2H), 1.24 (s, 2H), 1.05 (t, J = 6.5 Hz, 3H). ^{13}C NMR (101 MHz, DMSO-d_6) δ 159.06, 152.80, 149.75, 148.24, 146.85, 140.75, 133.60, 130.29, 128.98, 128.56, 126.97, 125.54, 124.77, 124.62, 124.20, 124.16, 124.02, 123.89, 123.27, 121.70, 119.41, 87.77, 87.04, 47.25, 38.50, 37.60, 26.81, 23.25, 20.82, 11.51. HRMS m/z: calcd for $C_{42}H_{38}N_3S^+$ [M−I]$^+$ 616.2781; found 616.2778 [M−I]$^+$. HPLC analysis: retention time at 2.800 min eluted with MeOH/H_2O = 50:50 (v/v), purity = 99%.

Water solubility analysis for the ligands

The determination of water solubility of ligands was performed by modifying the reported methodology (44). Briefly, ligands **1**–**4** were prepared into 10, 20, 30, 40, 50 μg standard solutions in ultra-pure water. A Diamonsil C18 column (250 × 4.6 mm, 5 μm) was used at room temperature with an elution using the mobile phase (MeOH/H_2O = 50:50 v/v) and the detection wavelength was 225 nm. Under these chromatographic conditions, the standard solution was determined with HPLC and the peak area corresponding to each concentration was recorded. The linear regression equation was obtained as follows: $Y = AX + B$ (Supplementary Table S7). The saturated aqueous solution of ligand (**1**–**4**) was put into an oscillator for 24 h, and then centrifuged for 15 min. The supernatant was diluted and then was determined with HPLC. The solubility was calculated with the regression equation established.

UV−visible and fluorescence assays

The UV−vis spectrum was obtained by using Lambda 25 Spectrophotometer (Perkin Elmer) in Tris buffer (10 mM Tris−HCl buffer containing 60 mM KCl). The fluorescence spectrum was recorded on a LS-45 fluorescence spectrometer (Perkin Elmer) in Tris buffer (10 mM Tris−HCl buffer containing 60 mM KCl). The colorimetric dish has a slit width of 1 mm and an optical diameter of 10 mm. The detection limit (LOD) was estimated by the fluorescence titration according to the formula: LOD = K (S_b/m). According to the International Union of Pure and Applied Chemistry (IUPAC), K value is generally taken as 3. S_b represents the standard deviation of blank multiple measurements (n = 20), and m is the slope of calibration curve, indicating the sensitivity of the method.

Downloaded from https://academic.oup.com/nar/article/50/4/1829/6528910 by guest on 04 March 2022

Determination of equilibrium binding constant with fluorescence titration

Fluorescence signal was measured at 25°C for the ligand (5 μM) and nucleic acid at different concentrations (0–18 μM) in a Tris−HCl buffer (10 mM, pH 7.4) containing 60 mM KCl. With the data obtained through fluorimetric titrations, the binding constants were analyzed according to the independent site model (45) by nonlinear fitting to the equation (46): $F/F_0 = 1 + (Q - 1)/2\{N + 1 + X - [(X + 1 + N)^2 4X]^{1/2}\}$. In this equation, $Q = F_{max}/F_0$, $N = (K_a C_{dye})^{-1}$, and $X = nC_{DNA}/(C_{dye})$, $K_d = K_a^{-1}$. The parameters P and M, Q and N were found via the Levenberg-Marquardt fitting routine in the Origin 9.0 software, whereas n was varied to obtain a better fit.

Job plot experiment

The total concentration of ligand and nucleic acid was fixed at 18 μM and the fluorescence signal intensity was measured for the concentration of ligand from 0, 1.8, 3.6, 5.4, 7.2, 9.0, 10.8, 12.6, 14.4, 16.2 and 18 μM (the nucleic acid concentration added was in the order from 18 to 0 μM). The well-mixed solution was then incubated at 4°C for 12 h before taking measurements. The fluorescence signal of each measurement was plotted as the vertical coordinate and the ratio of ligand concentration to the total concentration as the horizontal coordinate. The Gaussian fitting formula is used for data processing on Origin 9.0 software.

Measurement of fluorescent quantum yields of the new compounds

The fluorescence quantum yields of various compounds interacted with DNA were calculated according to the standard of fluorescein ($\Phi = 0.95$) in the condition of 1% NaOH ethanol (47). Five gradient increasing solutions were added to the fixed concentration of DNA solution, and the UV absorption value and fluorescence intensity value of each gradient concentration compound and DNA were recorded. The fluorescence quantum yield was calculated according to the following equation (48): $\Phi_x = \Phi_{ST}$ $(Grad_x/Grad_{ST})$ $(\eta^2{}_x/\eta^2{}_{ST})$, where the subscript ST is the standard, the subscript x is the test sample; represents the fluorescence quantum yield; Grad is the slope of the curve with the integrated fluorescence intensity as the ordinate, the ultraviolet absorbance as the abscissa, and η is the refractive index of the solvent.

Circular dichroism (CD)

The CD spectrum was measured by Chirascan spectrophotometer (Applied photophysics). Tris−HCl buffer (10 mM, containing 60 mM KCl, pH 7.4) was used to prepare G4–DNA solution as 5 μM. The ligand concentration was 10 μM. A quartz cuvette with a path length of 1 mm was used to record the spectral data in the wavelength range of 225–700 nm with a bandwidth of 2 nm, a step of 1 nm and a point of 0.1 s/point. The CD spectral data obtained were the average value of three scans. In addition, for the CD melting assays, the G4–DNA solution of Pu27 and Telo21 at 5 μM were prepared with Tris−HCl buffer (10 mM, containing 60 mM KCl, pH 7.4). The ligand (5 μM) was added to the mixture for CD melting. The data were recorded at an interval of 1°C in the range of 25–95°C with a heating rate of 1.0°C/min. Use Origin 9.0 for final analysis of data.

Isothermal titration calorimetry (ITC) measurements of ligand−DNA interactions

ITC experiments were carried out in MicroCal PEAQ-ITC (Malvern, USA) microcalorimeter. The solutions of different DNA sequences were pre-annealed in 25 mM KH_2PO_4, 60 mM KCl buffer (pH 7.4, containing 2% (v/v) DMSO) by heated to 95°C in water bath for 5 min. Then, it was cooled to 25°C and placed at 4°C overnight. The pre-annealed DNA sequence (20 μM) in buffer was kept in the sample cell and the ligand (400 μM) was filled in the syringe of a volume 40 μl with the same buffer. The ligand was mixed with the sample by stirring the syringe at 750 rpm at 25°C. There were 30 injections with a duration of 4 s and an interval of 150 s. Under the same conditions, the ligand was injected into the cells containing only buffer solution for a blank titration. The heat generated by the interaction was determined by subtracting the blank heat from the heat of ligand DNA titration. The binding enthalpy and other fitting parameters were determined by applying the built-in curve fitting model: One Set of Sites (MicroCal PEAQ-ITC (Malvern, USA)).

Fluorescence microscopy imaging study and staining effects

Fluorescence microscopy images obtained in MCF-7 cells (human prostate cancer cells, ATCC® CRL-1435) were recorded on confocal laser scanning microscopy (ZEISS LSM 800 with Airscan). The nucleus localization reference dyes used was Hoechst 33342 (1.0 μM). The concentration of ligand **2** or **3** used was 5 μM. The ligand was able to enter the cell quickly. The excitation wavelength of Hoechst 33342 was 405 nm and that of **2** or **3** was 488 nm.

Cell imaging of MCF-7 cells treated with RNase and DNase

MCF-7 cells were cultured on a confocal dish for 24 h. Before dyeing experiment, it was precooled with methanol (−4°C, 2 min), and then washed twice with PBS. In order to make the cell membrane permeable, cells were cultured with 1% Triton X-100 for 15 min and then washed with PBS thrice. The pretreated MCF-7 cells were stained with ligand **2** or **3** at 5 μM (25°C, 20 min). After washing with PBS for three times, one culture dish was treated with 100 μg/ml RNase (37°C, 2 h) and the other was treated with 100 μg/ml DNase (37°C, 2 h). Imaging experiments were carried out with a Zeiss LSM800 confocal laser scanning microscope.

Immunofluorescence experiments in MCF-7 cells

Confocal images of MCF-7 cells stained with ligand **2** (or **3**) and BG4: MCF-7 cells grown on a glass dish were fixed in 4% paraformaldehyde/PBS for 15 min, then infiltrated with 0.1% Triton-X 100/PBS at 37°C for 30 min,

Downloaded from https://academic.oup.com/nar/article/50/4/1829/6528910 by guest on 04 March 2022

and then blocked with 5% goat serum/PBS at 37°C for 3 h. Immunofluorescence tests were performed with standard methods. The glass dish was incubated with Anti-DNA/RNA G-quadruplex [BG4] (Ab00174-1.1, Absolute) for 3 h at 37°C. The glass dish was washed six times with blocking buffer and then incubated with DyLight™ 405 AffiniPure Goat Anti-Mouse IgG (H + L) (115-475-062, Jackson) for 3 h at 37°C. The glass dish was washed again with blocking buffer six times and then incubated with ligand **2** or **3** (2.5 μM) for 30 min. Finally, digital images were recorded using a ZEISS LSM 800 microscope and analyzed using ZEN software.

^{1}H NMR titration study

The oligomeric DNA solution at 300 μM was prepared with phosphate buffer (25 mM KH_2PO_4, 10% D_2O, 70 mM KCl, pH 7.4), heated to 95°C, annealed to room temperature, and incubated for 24 h. During the measurement, the ligand (**2** or **3**) with a concentration range of 300–600 μM were gradually added to the DNA solution for NMR analysis. The experiments were carried out at 25°C on a 600 MHz spectrometer (Bruker).

Molecular docking study

The NMR structure of a mutated c-MYC G-quadruplex (PDB 2MGN) was used to perform docking study on ligands **2** and **3**. The three-dimensional structure of small molecules was sketched with DS viewer 3.5. Autodock Tools (version 1.5.6) was used for converting structure files to pdbqt format (49). The docking study was carried out by using AutoDock Vina program (50). The dimensions of the active site box were chosen to be large enough to encompass the entire G4 structures. An exhaustiveness of 100 was used and other parameters were left as default.

RNA isolation and qRT-PCR

MCF-7 cells (ATCC® HTB-22) were cultured in six-well plates and then treated with different concentrations of ligands. After that, MCF-7 cells were continued to be cultured for 36 h. The medium was discarded and washed three times with PBS, 0.5 ml of triazole (Sigma-Aldrich) was added to lyse the cells for 3 min, and then 0.2 ml of chloroform was added. The mixture was stirred thoroughly and then centrifuged at 13 500 rpm for 15 min at 4°C to separate the aqueous phase containing RNA. Total RNA was precipitated from the aqueous phase with anhydrous isopropanol. The RNA precipitate was washed with 75% ethanol (containing 25% DEPC water) and then dissolved in 20 μl of redistilled distilled water without RNase. In order to remove the genomic DNA contamination in the isolated RNA, the samples were treated with DNase I and identified by polymerase chain reaction. The prepared RNA was therefore contained no genomic DNA. Then, the HiScript® II One Step qRT-PCR SYBR Green Kit was used for reverse transcription of RNA and quantitative analysis of transcribed cDNA. The concentration of RNA was 0.5–2 μg per reaction. The forward and reverse primer sequences for amplification were listed in Supplementary Table S2. The RNA was reverse transcribed and amplified by qRT-PCR (analytikjena, qTOWER2.2). A comparative Ct (ΔΔCT) method was used to compare the mRNA expression levels of genes of interest.

Western blot assay

The cells in the logarithmic growth phase were inoculated on the 6-pore plate and treated with ligand **2** or **3** for 36 h. The cells were collected and incubated on ice for 20 min in the RIPA buffer, then at 4°C, 12 000 × g for 20 min. The total protein concentration was quantified by BCA kit. The same amount of protein was loaded onto the SDS-PAGE gel and the separated protein was transferred to the PVDF membrane. After blocking with 5% skim milk, the membranes were incubated with primary antibodies against c-MYC (Affinity, AB_2834974, diluted 1:1000), hTERT (Affinity, AB_2839083, diluted 1:1000), γ-H2AX (Affinity, AB_2834619, diluted 1:1000), 53BP1 (Affinity, AB_2844517, diluted 1:1000), caspase-3 (Affinity, AB_2835170, diluted 1:1000), Bax (Affinity, AB_2833304, diluted 1:1000) and β-actin (Affinity, AB_2839420, diluted 1:1000) was used as a protein endogenous control. The membranes were washed three times with TBST buffer for 0.5 h, then incubated with Goat Anti-Rabbit IgG (H + L) HRP secondary antibody (Affinity, AB_2839429, diluted 1:5000) for 2 h. After washing with the TBST buffer for 0.5 h again, membranes were scanned with the ECL system (GE Healthcare).

Comet assay for DNA damage study

The collected MCF-7 cells (5×10^6 cells/ml) were suspended in 1 ml of PBS and 30 000 cells were taken and mixed with 75 μl of low melting point agarose (0.5% (w/v)). The mixture was placed on a glass microscope slide coated with normal melting point agarose (0.5% (w/v)), covered with a coverslip and cured at 4°C for 10 min; then, the coverslip was removed and covered with 75 μl of low melting point agarose. The samples were lysed in lysis solution (2.5 mol/l NaCl, 100 mmol/l Na_2EDTA, 10 mmol/l Tris (pH 10), 1% TritonX-100, 10% DMSO) for 1.5 h at 4°C. After lysis, the samples were immersed in alkaline buffer (1 mmol/l Na_2EDTA, 300 mmol/l NaOH, pH > 13) for 30 min. Then, electrophoresis was conducted at room temperature for 20 min (300 mA, 25V). The gel was finally neutralized with Tris (pH 7.5) and then stained with DAPI (1 μM/ml) for 10 min. Imaging was performed with an inverted fluorescence microscope (Olympus IX71, Japan).

Cellular uptake experiment

The uptake of ligand **2** or **3** by MCF-7 cells was studied using flow cytometry. MCF-7 cells were inoculated in 12-well plates and incubated for 12, 24 and 36 h with the addition of ligand **2** or **3** (1 μM). The medium was then removed, washed three times with pre-chilled PBS, followed by trypsin digestion and data analysis using a flow cytometer (BD FACSCanto™ II) for data analysis.

Downloaded from https://academic.oup.com/nar/article/50/4/1829/6528910 by guest on 04 March 2022

Telomerase inhibition assay (TRAP assay)

MCF-7 cells were left untreated or treated with ligands **2** or **3** for 36 h. The cells (1×10^6 cells) were re-suspended in 200 μl CHAPS lysis buffer and incubated on ice for 30 min. After centrifugation at 12 000 × g for 20 min, all supernatants were transferred to sterile enzyme-free tubes and stored in a refrigerator at −80°C. The trap assay is based on the classical method (51). PCR reactions: each 20 μl reaction system contained 1 μl of cell extract, 0.125 mmol/l dNTP mixture, 0.25 μmol/l TS primer (5′-AATCCGTCGAGCAGAGTT-3′), TRAP buffer (20 mM Tris–HCl, pH 8.3, containing 1.5 mM $MgCl_2$, 63 mM KCl, 0.05% (v/v) Tween 20, 1 mM EGTA, and 0.01% BSA), 0.25 μmol/l ACX primer (5′-GCGCGGC TTACCCTTACCCTTACCCTAACC-3′), 0.25 μmol/l NT (5′-ATCGCTTCTCGGCCTTTT-3′), and 0.01 amol/μl TSNT (5′-AATCCGTCGAGCAGAGTTAAAAGGCCG AGAAGCGAT-3′), ddH_2O, and 2 U Taq polymerase (Takara). The telomerase mixture was extended in a water bath at 30°C for 30 min and inactivated at 95°C for 5 min. PCR was performed for 30 s at 94°C, 30 s at 59°C, 1 min at 72°C for 31 cycles and 72°C for 5 min. PCR samples were separated on a 10% (w/v) native-PAGE gel in 0.5× TBE for 2 h at 120 V. After electrophoresis, the gel was stained with SYBR Gold for 30 min at room temperature and the images were captured with reverse processing.

qRT-PCR and ELISA assay in CA46 and Raji cell

The cells after treatment for 36 h with ligand **2** or **3** at different concentrations, the total RNA was extracted from CA46 and RAJI cells. The HiScript® II One Step qRT-PCR SYBR Green Kit was then used to reverse transcribe RNA and the generated cDNA was measured at a concentration of 0.5–2 μg of RNA per reaction. The forward and reverse primer sequences utilized to conduct the amplification (Exon1, Exon2, c-MYC and GAPDH) were listed in Supplementary Table S2. qRT-PCR was used to reverse transcription and amplification of RNA (analytikjena, qTOWER2.2). A comparative Ct (ΔΔCT) method was used to calculate gene mRNA expression levels. CA46 and RAJI cells were also treated with ligands **2** or **3** at different concentrations for 36 h. Cells were frozen and thawed many times before being centrifuged for 5 min (4°C, 3000 × g) and the supernatant was collected for detection with the Human Caspase 3(Casp-3) ELISA kit (MEIMIAN, MM-1550H1).

In vivo antitumor treatment

All animal experiments were performed in compliance with the Animal Management Rules of the Ministry of Health of the People's Republic of China. All animal experiments conducted in the present study were performed in compliance with the institutional ethics committee regulations and guidelines on animal welfare. The experiments were performed with 2% isoflurane to minimize suffering. In the study, female Balb/c nude mice (18–20 g) were placed in small animal isolators under aseptic conditions to obtain food and water freely. All animal care and procedures were approved by the university ethics committee for use in laboratory animals. To establish a xenograft model, MCF-7 cell suspension (5×10^6 cells) was injected subcutaneously. When the subcutaneous tumor diameter was 100 mm^3, female nude mice were divided into three groups: control group with tail vein injection of PBS (group 0), tail vein injection of ligand **2** (group 1), and tail vein injection of ligand **3** (group 2). The dose of ligand in the treatment group was 1.5 mg/kg, injected every three days. Mice were executed on the 18th day after intravenous ligand injection. The blood sample was collected and separated into cell and serum fractions by centrifugation for routine blood data, while major organ and tumor tissues were obtained from each group for hematoxylin and eosin (H&E) staining, TUNEL staining and Ki67 staining.

Analysis of ligand concentration in blood

Ligand **2** or **3** was injected into Sprague–Dawley rats (female, weighing 200 ± 20 g) via tail vein (0.5 ml, 1.5 mg/kg) and blood samples (0.3 ml) were collected from the orbital sinus at 5 min and 1, 2, 4, 8, 12 and 24 h post-injection, respectively. The blood sample collected was centrifuged at 4000 × g for 10 min to collect plasma and placed at −80°C for further use. The preparation of standard concentration gradients of the ligand was conducted as follows. A stock solution of 0.5 mg/ml ligand (**2** or **3**) was prepared using dimethyl sulfoxide (DMSO) and then different working concentrations of the ligand (0.24, 0.49, 0.98, 1.95, 3.91, 7.81, 15.6 μg/ml) were prepared by serial dilution of the stock solution with methanol/water (9:1) solution. 10 μl of the working solutions of ligand **2** or **3** (from 0.24 to 12.5 μg/ml) was added to 100 μl of plasma for blank group. The prepared solutions were placed at −80°C for further analysis. Thiazole orange (Sigma-Aldrich, 390062) was used as the internal standard and a working concentration at 0.625 μg/ml was prepared. To the samples prepared for calibration and the blood samples collected from rats to be analyzed, 880 μl acetonitrile and 10 μl internal standard solution (Thiazole Orange, 0.625 μg/ml) were added. The resulting solution was vortexed for 30 s and the supernatant was collected by centrifugation at 10 000 × g for 10 min and then was analyzed with LC–MS (Thermo Fisher, TSQ Endura).

Statistical analysis

Statistical details including the number of biological replicates (N) and P values are detailed in figure legends. Data in bar graphs are shown as an absolute number with means ± SD noted. Wilcoxon-Mann-Whitney test was used to calculate significant differences where indicated. $P < 0.05$ was considered statistically significant; ns, not significant. The criterion for statistical significance was taken as ns: $P > 0.05$, $^{*}P < 0.05$, $^{**}P < 0.01$, $^{***}P < 0.001$.

Data availability

The main data supporting the results in this study are available within the paper and Supplementary Information. The raw and analyzed datasets generated during the study are

Downloaded from https://academic.oup.com/nar/article/50/4/1829/6528910 by guest on 04 March 2022

too large to be publicly shared but are available for research purposes from the corresponding authors on reasonable request.

RESULTS

Design of ligands for the understanding of structural influence targeting G4-structures

The red fluorescent G4-binding ligands built on a non-selective thiazole orange (**TO**) scaffold (52) were systematically engineered to demonstrate the critical structural influence in the discrimination between two vital classes of G4-structures of c-MYC Pu27 and telomeric Telo21 (Figure 1). Some recent studies have shown that modification at the 2-position of 1-methylquinolinium moiety of **TO** could induce selectivity toward telomeric G4-structures, particularly Telo21 (53,54). However, how to design a ligand that selectively recognizes the G4-structures of a promoter over the telomeric ones remains an open question. The challenge is due to the high similarity of the G-tetrad binding pocket among G4-structures. To address this challenge, we aimed to develop a series of small ligands to study the structural influence in the discrimination between the G4-structures of c-MYC promoter and telomere in molecular recognition. Our approach is to design multi-site interactions, which is able to target the binding sites of the G-quartet, loops and flanking nucleotides at either 3′- or 5′-terminal in two-direction. It is because the sequences of loops and flanking residues of monomeric G4-structures could offer a much greater difference than a single G-tetrad scaffold.

In order to design a molecular system that offered multi-site interactions targeting the G4–DNA binding pocket, we constructed ligands with special substituent groups through two directions (Figure 1): a substitution at the site of the nitrogen atom of the thiazole-ring linked with a flexible polar amino group (propylpyrrolidine) and at another site with the substitution at the 2-position of 1-methylquinolinium fragment to regulate the polarity, rigidity, and the size of the substituent group. These two flexible substituent groups that are extended from the rigid **TO** scaffold could provide extra interactions with the G4-binding pocket, such as hydrogen bonding and/or π–π interactions with the loop or flanking nucleotides in two directions. The central large π–conjugation aromatic system (**TO** scaffold) could offer notable interactions on the G-tetrad surface through π–π stacking with the planar guanine bases of G4-structures. We speculated that selectivity toward c-MYC or telomeric G4-structure could be tunable by regulating different modes of interactions, such as hydrogen bond and aromatic π–π stacking, with respect to the binding environments through multiple sites inside the rigid G4-pocket. The present study demonstrated a new strategy in ligand design for fluorescent recognition of G4-structures of c-MYC and telomere.

Study of binding selectivity of ligands toward different types of G4-structures

The photophysical property of the ligands was summarized in Supplementary Table S3 and Figure S2. To understand the structural effects and multi-site interactions attributed to the substituent groups integrated in the thiazole orange scaffold, ligands **1–4** were screened with 20 representative nucleic acids, including single-stranded, duplex and triplex DNA, G-quadruplex DNA (c-MYC promoter and telomeric), and rRNA, in a pH 7.4 Tris–HCl buffer solution. The induced fluorescence intensity of DNA-ligand interaction indicated the degree of selectivity of each ligand toward the G4-structures (Figure 2 and Supplementary Figure S3). All ligands displayed negligible background fluorescence without nucleic acids. The fluorescence titration results showed both **TO** and **1** generated strong signal with most substrates (Supplementary Figure S3A, D) while the single-stranded DNA (dT21) showed very weak signal. The results revealed that these two ligands were non-selective. Moreover, the main structural difference between **1** and **TO** is the flexible propylpyrrolidine group of **1** replacing the methyl group of **TO** at the nitrogen atom of thiazole ring. Interestingly, **1**, which has a more flexible propylpyrrolidine group, could also induce strong fluorescent signals similar to those observed in **TO**. We speculated that this might be due to an extra interaction site with the nucleotides provided by the amino group from the propylpyrrolidine, possibly through hydrogen bonding, that offered better restriction on intramolecular torsional motion of the rotatable benzothiazole and 1-methylquinolinium fragments. In addition, this extra interaction site also granted **1** a little observable selectivity (∼1.7-fold) among the promoter G4–DNAs compared to **TO**. We therefore speculated that it could be feasible to enhance the selectivity further through the engineering of substituent groups that could offer multi-interaction sites (apart from the common π–stacking interaction with G-tetrad motif) for better matching with the spatial environment of the subtle G4-structures.

Ligand **2** that is constructed based on **1** has a *p*-dimethylaminostyryl group at the 2-position of 1-methylquinolinium scaffold and is connected through a relatively rigid ethylene bridge. This *p*-dimethylaminostyryl group could create a second interaction site, which is in the opposite direction to the flexible propylpyrrolidine group of **1**. The overall structure of **2** could potentially offer two-directional three-site interactions at the G4-binding pocket, which include the interaction of **TO** fragment with the G-tetrad (π–π stacking) and two extended amino groups (one flexible, one rigid) for hydrogen bond interactions with polar residues of the binding pocket. The performance of G4-structure discrimination was determined by whether the integrated substituent groups could fit to the spatial environment of the binding pocket. The ligand design is thus able to probe a small structural difference between various G4-structures and, more importantly, the difference may be primarily due to different flanking nucleotides and loop sequences of G4-structures.

The selectivity of **2** toward various nucleic acid substrates was improved markedly (Supplementary Figure S3B) and the ligand showed excellent fluorescent discrimination targeting telomeric G4–DNA, particularly Telo21. The interaction signal from dsDNA and the G4s of promoter was less than one-fourth of that from Telo21. All other nucleic acid substrates including ssDNA, triplex DNA and rRNA induced even much weaker signal. The results support our hypothesis that the two-directional multi-site interactions may provide good recognition ability for G4-structures. The dis-

Downloaded from https://academic.oup.com/nar/article/50/4/1829/6528910 by guest on 04 March 2022

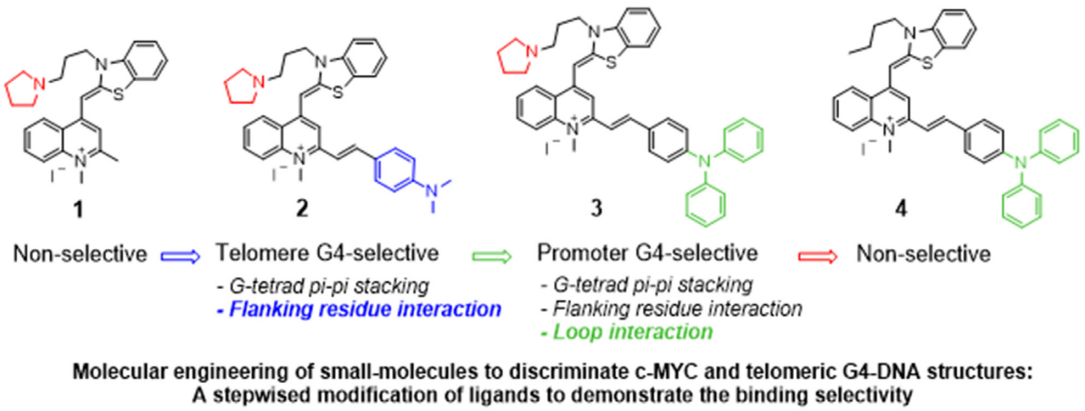

Figure 1. The design of G4-selective fluorescent binding ligands offering three-point interactions via the molecular engineering of a non-selective thiazole orange scaffold. The thiazole orange derivative **1** is non-selective. The critical site at the 2-position of the 1-methylquinolinium moiety of **1** is modified to regulate the polarity, rigidity, and the size of the ligand in order to achieve high discrimination ability between c-MYC promoter and telomeric G4–DNA structures. Ligand **2** bearing a terminal *p*-dimethylaminostyryl group is selective toward telomeric G4–DNA (Telo21, 4Telo, Human12, Oxy12 and Htg24). Ligand **3** bearing a terminal *p*-(diphenylamino)styryl group is selective toward c-MYC G4–DNA (Pu27, Pu24, Pu22 and Pu18). Ligand **4** without the polar propylpyrrolidine group linked to the thiazole-ring loses selectivity toward G4–DNA structures, indicating the importance of two-directional and multi-site interaction design in the ligands **2** and **3**.

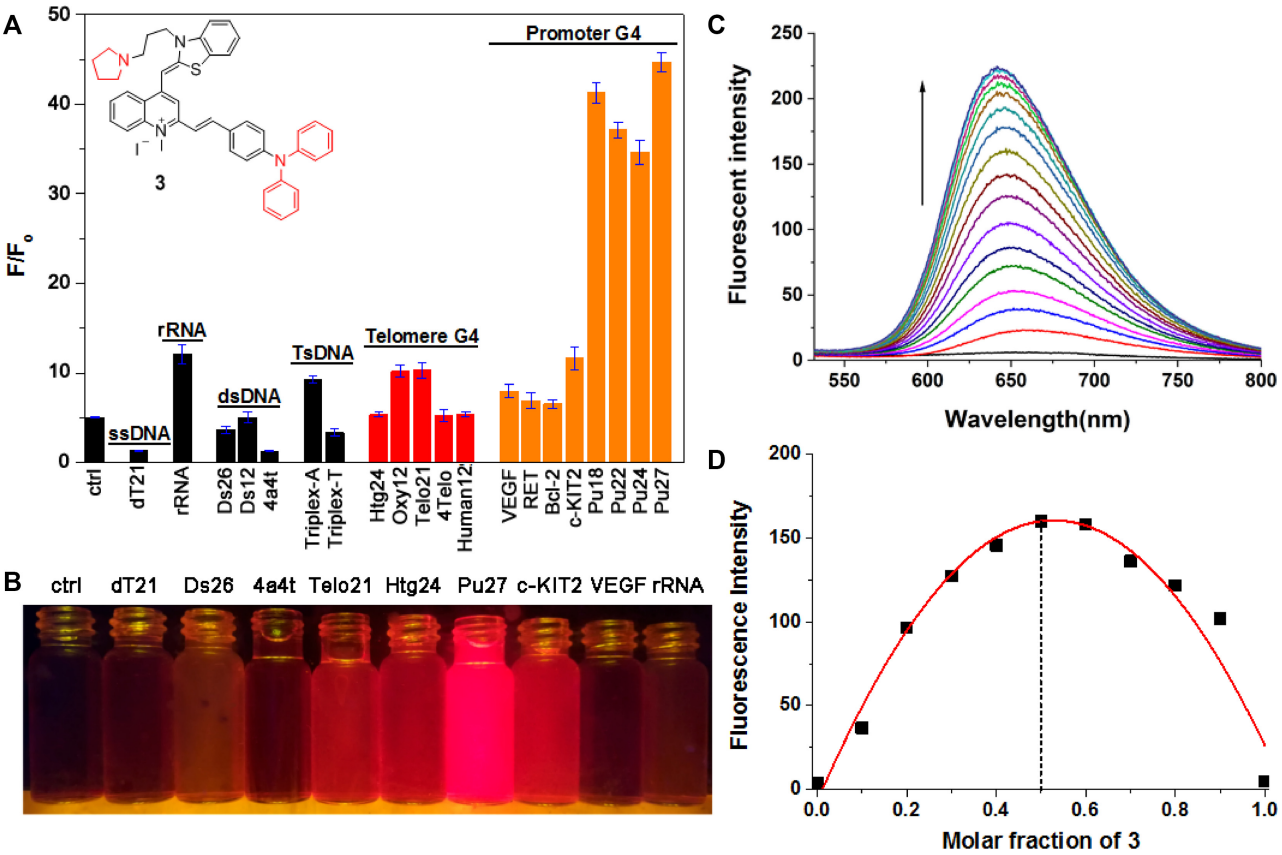

Figure 2. The selectivity of **3** to recognize G4–DNA to induce fluorescence signal. (**A**) Selectivity screening based on induced fluorescent responses of **3** upon binding to various nucleic acids in a Tris–HCl buffer (10 mM, pH 7.4, containing 60 mM KCl). Concentration of ligand is 5 μM with 18 μM DNA. The control is a test solution containing the same concentration of ligand but without the addition of DNA substrates. (**B**) Fluorescence signal **3** (5 μM) observed directly under a laboratory UV-chamber (illuminated at 302 nm) upon the addition of nucleic acids (18 μM) in a Tris–HCl buffer (10 mM, pH 7.4, containing 60 mM KCl). (**C**) Fluorescence titration spectra of **3** (5 μM) with Pu27 G4–DNA (0–18 μM) in a Tris-HCl buffer (10 mM, pH 7.4, containing 60 mM KCl). (**D**) The Job plot analysis of the binding stoichiometry of **3**-Pu27.

Downloaded from https://academic.oup.com/nar/article/50/4/1829/6528910 by guest on 04 March 2022

crimination could be directly correlated with the unique G4 characteristic (sequence) of the binding environment. The interaction results obtained with **2** (Supplementary Figure S3B) suggested that the spatial environment of the binding pocket of telomeric G4–DNA such as Telo21 and 4Telo could be significantly different from that of promoter G4s including c-MYC (Pu27, Pu24, Pu22 and Pu18), Bcl-2, c-KIT2, RET and VEGF. The c-MYC G4–DNA structure could have many isomers but its topology is primarily in parallel conformation and there are only a few flanking bases at the 5′- or 3′-terminal (12). However, the topology of telomeric G4 is more complicated because most telomeric sequences, such as Htg24 and Telo21, form hybrid-type conformations in the presence of K^+ ions (9). Moreover, the propeller loop and lateral loop were found in the hybrid-type telomeric G4. The lateral loop and flanking bases are in the 5′ or 3′-terminal (13). We therefore speculated that the crucial structural difference of G4s for the selectivity might probably come from the sequences of the flanking nucleotides (5′- or 3′-terminal) and/or the loops. The approach of developing ligands with the function of multi-site interaction could tailor a molecular scaffold highly matching the unique G4-structure.

To probe the structural characteristics of c-MYC G4–DNA and discriminate c-MYC G4s from telomere with ligands, we tried to vary the substituent groups at the thiazole ring through *N*-substitution and at the 2-position of 1-methylquinolinium in a two-directional manner. We eventually identified ligand **3** bearing a *p*-(diphenylamino)styryl substituent group that has two rotatable phenyl rings rather than methyl groups (ligand **2**) and that possessed excellent fluorescent discriminatory ability toward c-MYC G4–DNA structures including Pu27, Pu18, Pu22, and Pu24 against telomeric G4, Bcl-2, c-KIT2, RET, VEGF and other non-G4 nucleic acids (Figure 2A). *In vitro* binding assay showed that the **3**-Pu27 interaction induced a fluorescence intensity ∼4–5-fold higher than the telomeric G4 substrates tested. Surprisingly, the binding preference of **3** (c-MYC G4-selective) was opposite to that of **2** (telomeric G4-selective). The excellent selectivity of **3** toward c-MYC G4-structures is important and meaningful because the c-MYC G4-selective small molecules are very attractive to anticancer therapeutics (55,56). Our newly developed ligand system could provide important insights into molecular drug design targeting the G4-structures of c-MYC.

To further prove the critical importance of two-directional multi-site interactions of the ligand system, we designed ligand **4** without the pyrrolidinyl group extended at the direction from the thiazole ring. The selectivity of **4** toward c-MYC G4-structures was completely disappeared (Supplementary Figure S3C). This ligand also showed poor discrimination between dsDNA and the G4-structures of telomere and c-MYC promoter. Moreover, by comparing the structure-discrimination relationship of **2**, **3** and **4**, we came to the conclusion that the two substituent groups, pyrrolidinyl group extended from thiazole ring and *p*-(dimethylamino)styryl or *p*-(diphenylamino)styryl group at the 2-position of 1-methylquinolinium, may be essential for the high selectivity toward either c-MYC or telomeric G4-structure over other types of nucleic acids. To understand more about the interaction mechanism of **3** with the c-MYC G4-structure, equilibrium binding study, CD measurements, G4-stabilization ability by T_m measurements, dynamic interaction study with ^{1}H NMR, and molecular docking study were performed.

In the *in vitro* binding study of **3** (Supplementary Figure S4, Figure S5 and Figure S7), only c-MYC promoter G4–DNAs including Pu27, Pu24 and Pu22 induced strong interaction signal, while the telomere G4s and other promoter G4–DNAs including Bcl-2 and c-KIT2, and the non-G4 nucleic acids showed much weaker interaction signal. It was found that the maximum fluorescence intensity of the **3**-Pu27 complex was almost 5 times as high as that of other G4 substrates under the same conditions. A linear relationship for the interaction was established (Supplementary Figure S6) and the limit of detection was estimated to be 97.5 nM. Therefore, **3** could be utilized as a sensitive and selective fluorescent tool for real-time detection and visualization of Pu27 (Figure 2B). In addition, the equilibrium binding constants of **3** with the representative DNAs were determined based on fluorescence titrations (Supplementary Table S4). The equilibrium binding constant (K) of **3**-Pu27 was found to be the largest ($K = 18.91 \times 10^5$ M^{-1}), while that of Telo21 was much weaker ($K = 6.88 \times 10^5$ M^{-1}), indicating that the interaction of **3**-Pu27 was stronger and the interaction mode could be different from that of **3**-Telo21 (Supplementary Figure S7). In the case of ligand **2** (Supplementary Figure S8), the interaction of **2**-telo21 ($K = 30.17 \times 10^5$ M^{-1}) was much stronger than that of **2**-Pu27 ($K = 14.26 \times 10^5$ M^{-1}). Moreover, the equilibrium dissociation constants (K_d) determined with isothermal titration calorimetry (ITC) (Supplementary Table S5, Figures S20 and S21) were found to be comparable to those obtained in fluorescence titrations. Furthermore, the competition experiments (Supplementary Figure S9) could support that **3** was selective toward Pu27 and had much higher binding affinity than duplex DNA (ds26), while **2** was selective toward telo21 over ds26. For **1** and **4**, similar equilibrium binding constants were obtained from the binding study with various substrates (Supplementary Figure S10), indicating their selectivity was poor because these two ligands could not offer two-directional multi-site interactions.

The study of ligand–G4 DNA interactions

In solution, the binding stoichiometry of **3**-Pu27 complex formed *in vitro* was found to be 1:1 (Figure 2D and Supplementary Figure S11). To understand the dynamic binding modes in solution for ligands **2** and **3** interacting with c-MYC and telomeric G4–DNA, ^{1}H NMR studies were conducted. The formation of G-tetrad gave a set of guanine imino protons that show characteristic chemical shifts in the 10–12 ppm region (57). Changes in these imino proton signals could be observed when the ligand interacted with the guanine (58). Since the chemical shifts of imino peaks of Pu22 (c-MYC) and Htg24 (telomeric) G4–DNA had been well resolved (59,60), we therefore selected these substrates for investigation. The interaction of **3** with Pu22 (Figure 3A), the imino proton peaks corresponding to the guanine bases G13, G4, G17, G10, G19, G15 and G6 were influenced whereas other imino proton signals did not show any notable changes. This indicated that **3** could in-

Downloaded from https://academic.oup.com/nar/article/50/4/1829/6528910 by guest on 04 March 2022

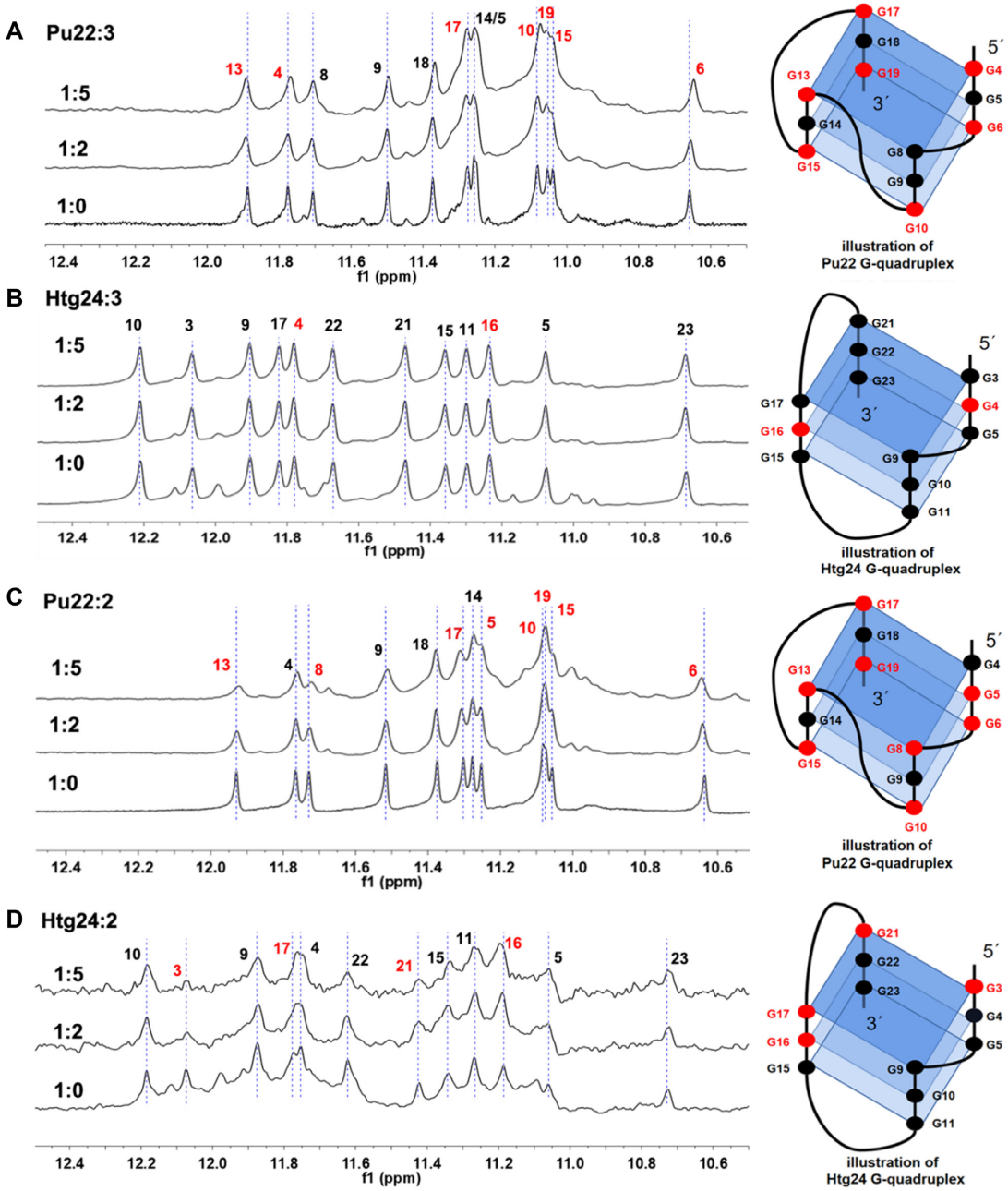

Figure 3. Chemical shift perturbation analysis of G-quadruplexes with ligands **2** and **3**. (**A**) Imino proton regions of the ^{1}H NMR spectra of Pu22 with ligand **3** at molar ratios from 1:0 to 1:5. (**B**) Imino proton regions of the ^{1}H NMR spectra of Htg24 with ligand **3** at a molar ratio from 1:0 to 1:5. (**C**) Imino proton regions of the ^{1}H NMR spectra of Pu22 with ligand **2** at molar ratios from 1:0 to 1:5. (**D**) Imino proton regions of the ^{1}H NMR spectra of Htg24 with ligand **2** at molar ratios from 1:0 to 1:5. The assays were performed in 25 mM KH_2PO_4 buffer (70 mM KCl, 10% D_2O, pH 7.4) using 600 MHz Bruker spectrometers at 25°C.

teract with the G-tetrad at 5′-terminal or 3′-end. For titration with telomeric G4, even at high ligand concentration (Htg24:**3** = 1:5), there were no notable changes observed for the imino proton signals, which might indicate that the interaction of **3**-Htg24 complex is weaker compared to that of **3**-Pu22. Moreover, for ligand **2**, the **2**-Htg24 interaction induced relatively strong signal influence to three sets of imino protons corresponding to G3, G17 and G21 located in G-tetrad at 5′-terminal. For the interaction of **2**-Pu22, the imino proton signals of G13, G8, G17, G5, G10, G19, G15 and G6 were influenced, which could indicate that the G-tetrad of both 5′- and 3’-end had interacted with the ligand. Taken together, despite the small perturbation on the chemical shift of imino protons, the ^{1}H NMR study could suggest a stacking interaction with the terminal G-tetrad.

Molecular docking study was performed using an NMR structure of c-MYC G4 (PDBID: 2mgn) (61) to predict the possible site and mode of interaction for ligand **3**. The bind-

Downloaded from https://academic.oup.com/nar/article/50/4/1829/6528910 by guest on 04 March 2022

ing modes that were most consistent with the NMR observation of the end π–stacking interaction were depicted. The possible interaction differences between **2** and **3** in the model were compared. Upon binding to c-MYC G4, the π–conjugation system of **2** that arose from the **TO** scaffold and the styryl moiety contributed to the π–π stacking interaction with two guanines (G4 and G8) within the G-quartet (Supplementary Figures S12A and B). The nitrogen atom of pyrrolidine formed a hydrogen bonding interaction with the phosphate backbone of the flank residues. For the docking study of **3**, which was more selective than **2** toward c-MYC G4–DNA, the π–conjugation system arising from **TO** and styryl moieties also contributed to the π–π stacking interaction with G4 and G8 within the G-quartet (Supplementary Figure S12C and D). Similarly, the pyrrolidine group was also found to have formed a hydrogen bonding interaction with the phosphate backbone of the flank residues. More importantly, the diphenylamino group of the styryl substituent was found to have extended into the loop near G13 and engaged in hydrophobic interactions with A12. The terminal non-polar diphenylamino substituent group of **3** could play a role in the selective recognition of the c-MYC G4-structure.

The multi-site interactions including π–π stacking, hydrogen bonding and loop interactions could rigidify the π–conjugation system of **3** and thus the ligand was able to provide good structural discrimination among G4-structures. The strong fluorescence signal enhancement observed in **3**–G4 complex could be attributed to the interaction with G4-binding pocket (a rigid environment) that restricted the intramolecular rotation of **3** and that suppressed the non-radiative decay of the ligand. To illustrate this, the degree of the enhancement of fluorescence of the ligand in a glycerol-water medium with increasing viscosity was examined (Supplementary Figure S13). The results showed that the enhanced fluorescence intensity of the ligand was directly related to the viscosity of the medium, which could imply that the formation of **3**–G4 complex may restrict the intramolecular rotation and induce strong fluorescent recognition signal.

Imaging and co-localization of G4–DNA structures in MCF-7 cells

Live cell imaging and co-localization study targeting G4-structures using ligands **2** and **3** in MCF-7 cells were carried out. A commercial dye Hoechst 33342 was co-stained for comparison in the bio-imaging experiments (Figure 4A and Supplementary Figure S15). The double-stranded DNA stained by Hoechst 33342 gave a bright blue signal all around the nucleus. The green ($\lambda_{ex} = 488$ nm) imaged area stained by **3** was much less than that of Hoechst 33342. Ligand **3** only selectively stained certain regions including the area around the nuclear membrane, nucleus (few spots) and subnuclear structures (probably nucleoli). The results suggested that these regions could contain G4-structures. The enzymatic digestion assays using DNase and RNase (Figure 4B, C) confirmed that the substrates stained with **3** were DNA and not RNA.

To verify the G4-structures imaged by **3** in MCF-7 cells, a fluorescent-labeled antibody (BG4) was utilized to co-localize with the ligand in cells (62–64). The confocal images (Figure 4D) showed that the BG4 staining revealed the punctate fluorescence signal (blue foci) primarily in nuclei and some thinly foci were dispersed or scattered in cytoplasm, while **3** showed fluorescent spots in the nucleus and intensive signals in the subnuclear region that presumably was nucleoli. The merged image highlighted the co-localized foci, which supported that BG4 and **3** could have the same or similar cellular targets. In addition, we used BRACO19 to compete with **2**, **3** and **TO** in MCF-7 cells, respectively (Figure 5). After the MCF-7 cells were treated with BRACO19, both **2** and **3** showed obvious fluorescence reduction, particularly in the nucleus. The results indicated that the two ligands could have the same binding targets in cells. In contrast, due to the non-selective nature of **TO**, in the displacement assay, the double-stranded DNA also stained by **TO**, the difference observed in cell imaging was not obvious compared to **2** and **3**.

Study of ligand effects on cytotoxicity, gene expression and DNA damage in cancer cells

As indicated by the melting temperature experiments, both ligands **2** and **3** could stabilize the G4–DNA structures of c-MYC and telomere (Supplementary Figure S16), which could be able to repress cancer-related genes expression. The results showed a $\Delta T_m = 7.4°C$ for **3**–Pu27 complex, which was higher than that of **3**-Telo21 ($\Delta T_m = 3.3°C$). The ΔT_m results could indicate that **3** could stabilize Pu27 better than Telo21. To evaluate the anticancer activity of ligands **2** and **3**, four human cancer cell lines (U87, MCF-7, HeLa and PC3) and two nonmalignant human cell lines (HK-2 and 16HBE) were selected for cytotoxicity evaluation with MTT assays. According to the results shown in Figure 6A and B and the IC_{50} values summarized in Supplementary Table S6, **2** and **3** exhibited comparable cytotoxicity against the cancer cells examined with IC_{50} values ranging from 4.2–6.6 μM. The IC_{50} of the nonmalignant cells were found in the range of 8.5–19.1 μM.

The human telomerase gene telomerase reverse transcriptase (hTERT) is important for cancer and aging (65). Many studies have revealed that c-MYC could play a vital role in the regulation of endogenous hTERT gene expression (66,67). Even though the regulatory mechanism of hTERT is not fully understood, it is believed that the downregulation of hTERT expression could induce senescence in cancer cells (68). We found that ligand **2** showed better interaction than **3** with the hTERT promoter G4 *in vitro* (Supplementary Figure S14). We therefore compared their effects on the downregulation of c-MYC and hTERT gene expression in MCF-7 cells (Supplementary Figure S17). The results (Figure 6C, D) showed that both ligands at 10 μM were notably downregulated the expression level of c-MYC and hTERT mRNA. Ligand **3** also downregulated the telomerase RNA component (hTERC) mRNA expression level. Moreover, the downregulation of hTERT by the ligands **2** and **3** increased apoptosis and induced senescence of MCF-7 cancer cells (Figure 6E and F). After MCF-7 cells were treated with **2** or **3** for 36 h, hTERT was downregulated. In addition, both Caspase-3 and Bax activities were increased. The results indicated that the ligands induced

Downloaded from https://academic.oup.com/nar/article/50/4/1829/6528910 by guest on 04 March 2022

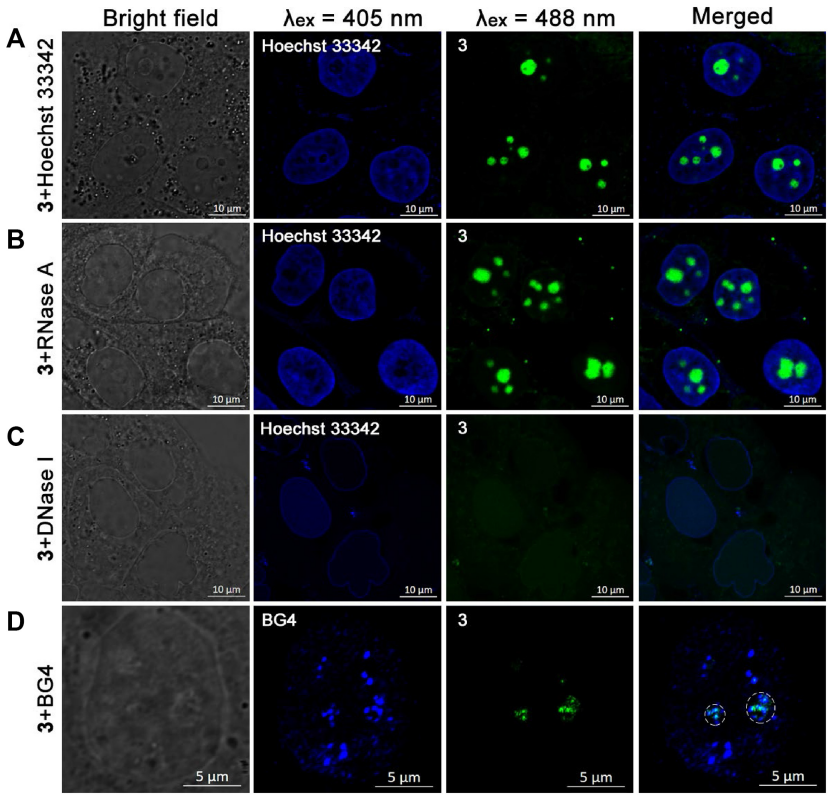

Figure 4. Imaging of G4–DNA with ligand **3** in cells. (**A**) Confocal microscope fluorescence images of live MCF-7 cells stained with 5 μM **3** for 30 min and 1.0 μM Hoechst 33342 for 10 min. The magnification is 40x in all pictures. (**B**) Confocal microscope fluorescence images of live MCF-7 cells stained with 5 μM **3** for 30 min and then the cells were treated with RNase A. (**C**) Confocal microscope fluorescence images of live MCF-7 cells stained with 5 μM **3** for 30 min and then the cells were treated with DNase I. (**D**) Confocal images of MCF-7 cells stained with 2.5 μM **3** and BG4 in the immunofluorescence experiments.

apoptosis (69,70). The western blot results obtained also indicated a positive correlation with the degrees of senescence induction in MCF-7 cells after the treatment with the ligands (Figure 6G). Furthermore, the ligands upregulated γ-H2AX and 53BP1, which were a characteristic DNA double-strand break response (71,72). These results were also found consistent with the DNA damage observed in MCF-7 cells after treatment with the ligands (Figure 6H). To compare the inhibitory effects of **2** and **3** on telomerase activity, TRAP assays were performed. The results (Figure 6I) showed that the activity of telomerase in MCF-7 cells was inhibited in a concentration-dependent manner for both ligands. Nonetheless, ligand **2** (telomeric G4-selective) at 10 μM showed better inhibitory effects than **3** (c-MYC G4-selective).

The study of ligand effects on exon-specific assays in CA46 cells

It was reported that over 85% of MYC expression was controlled by the G4 located prior to exons 1 and 2 in the promoter in most cancer cells (25). To further demonstrate that **3** was c-MYC selective, we studied the ligand effect on Exon-specific assays in RAJI and CA46 cells to demonstrate the specific MYC G4-ligand targeting the G4 within the nuclease hypersensitive element III_1 region (NHE III_1) of the MYC gene (73). A translocation between an immunoglobin chain (the IgH heavy chain that resides on chromosome 14) and the MYC promoter on chromosome 8 define Burkitt's lymphoma and cause aberrant control and upregulation of MYC expression. To study the effect of the ligand targeting c-MYC G4, a pair of Burkitt's lymphoma cell lines (RAJI and CA46) was utilized where the translocation caused the loss of the G4 region in the CA46 cell line, but not in the RAJI cell line. The cytotoxicity results (Figure 7A) showed that **3** had low IC_{50} values for both CA46 ($IC_{50} = 1.95 \pm 0.21$ μM) and Raji cells ($IC_{50} = 0.73 \pm 0.06$ μM). It is noteworthy that the semi-inhibitory concentration found in CA46 cells is about 3-fold higher than that in the Raji cells, which may be due to the chromosomal (8:14) translocation in CA46 cells (74). To correlate these two results, both RAJI and CA46 cells were treated with **3** at IC_{50} concentration for 36 h, followed by qPCR experiments on Exon 1, Exon 2, and the c-MYC gene (Figure 7B, C and Supplementary Figure S24). The results showed that ligand **3** had a significant inhibitory effect on Exon 1, but not on Exon 2, in CA46 cells. Moreover, most c-MYC expression was derived from Exon 2 and the suppression of c-MYC gene was weak in CA46 cells after treatment with the ligand. However, **3** showed remarkable suppression of Exon 1, Exon 2, and c-MYC in Raji cells. The c-MYC-lowering effect could be attributed to the ligand mediation through

Downloaded from https://academic.oup.com/nar/article/50/4/1829/6528910 by guest on 04 March 2022

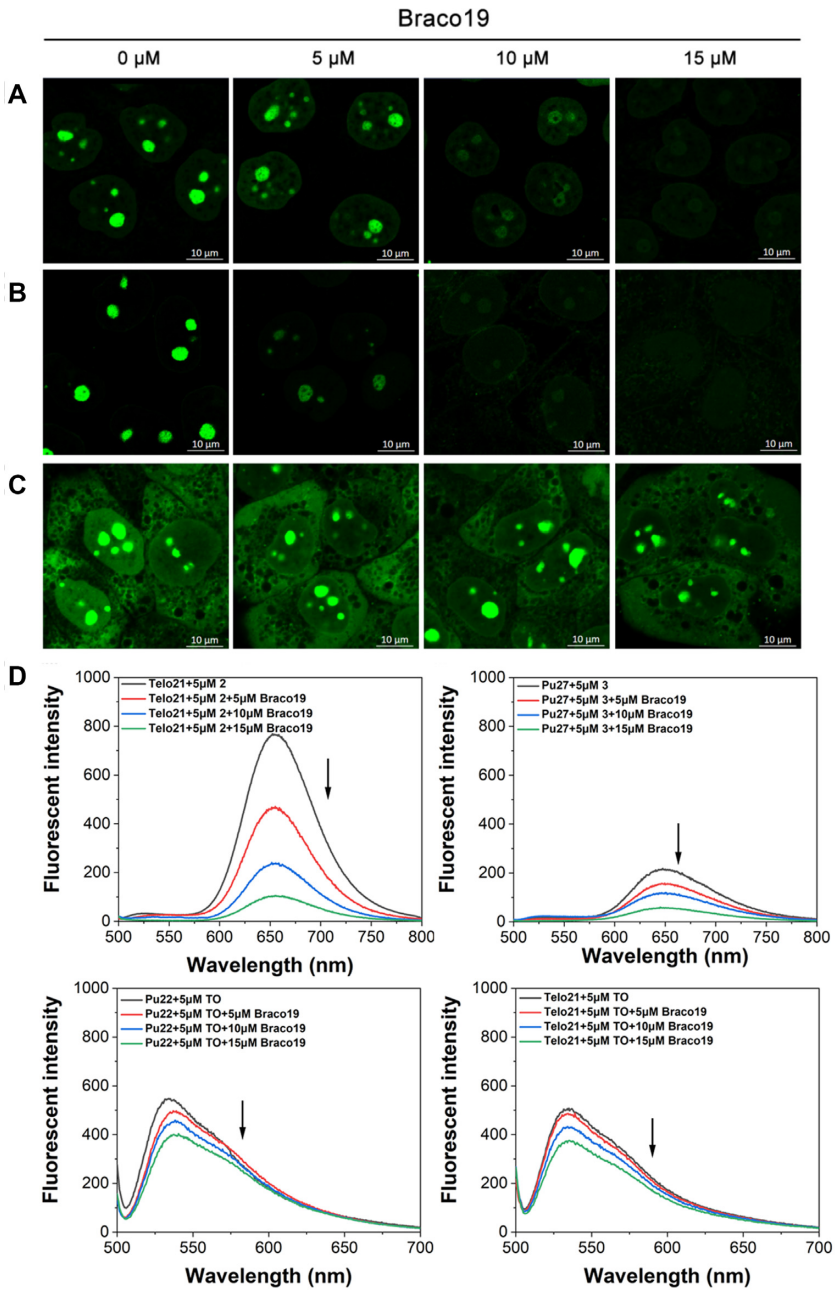

Figure 5. Confocal fluorescence images of MCF-7 cells stained with ligand **2**, **3** or **TO** (5 μM) with increasing BRACO19 (0–15 μM) displacement. (**A**) MCF-7 cells stained with **2** and BRACO19 (0–15 μM). (**B**) MCF-7 cells stained with **3** and BRACO19 (0–15 μM). (**C**) MCF-7 stained with **TO** and BRACO19 (0–15 μM). The cells were imaged using an LSM 800 laser scanning confocal microscope. The excitation wavelength was 488 nm for **TO** and **2** and **3**. (**D**) The competition study of fluorescent signal responses of **2**, **3** or **TO** (5 μM) binding with nucleic acid and increasing BRACO19 (0–15 μM).

the c-MYC G4-structure. On the contrary, ligand **2**, which was more selective to telomeric G4–DNA, was found to have less influence (Supplementary Figures S22 and S23). Furthermore, we examined the stimulation of apoptosis by ligand **3** at IC_{50} concentration for 36 h using caspase-3 activation assays for both RAJI and CA46 cells. The ligand exhibited a concentration-dependent increase in caspase-3 activation (Figure 7D) for both cells and the increase in the level in Raji cells was found to be twice higher than that in CA46 cells.

In vivo antitumor activity of ligands in MCF-7 tumor-bearing mice

The *in vivo* antitumor activity of **2** and **3** was investigated. Three groups of MCF-7 tumor-bearing female Balb/c nude mice were intravenously injected with PBS (group 0), ligand **2** (group 1) or ligand **3** (group 2) once every three days (Figure 8A). There was no weight loss in the three groups of mice throughout the experimental period (Figure 8B). Tumor growth in the treatment groups (groups 1 and 2) was

Downloaded from https://academic.oup.com/nar/article/50/4/1829/6528910 by guest on 04 March 2022

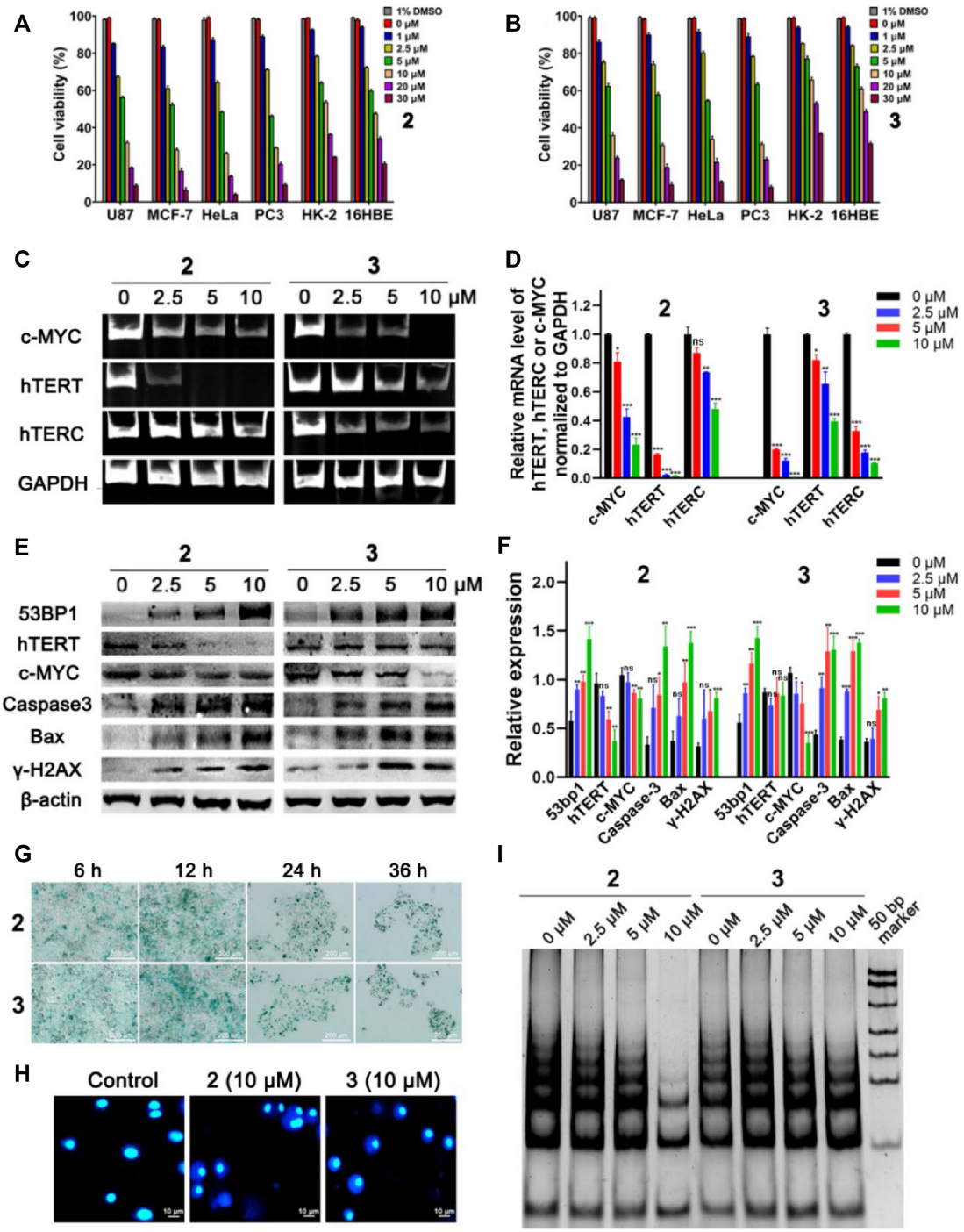

Figure 6. Cytotoxicity of ligands, gene expression and DNA damage studies. (**A**) U87, MCF-7, HeLa, PC3, HK-2 and 16HBE cells treated with **2** (1–30 μM) for 36 h, respectively ($N = 3$, mean ± SD). (**B**) U87, MCF-7, HeLa, PC3, HK-2 and 16HBE cells treated with **3** (1–30 μM) for 36 h, respectively ($N = 3$, mean ± SD). (**C**) qRT-PCR products obtained from MCF-7 cells were separated by electrophoresis in 3% agarose gel and stained with SYBR Gold. (**D**) The mRNA expression of hTERT, hTERC and c-MYC genes in MCF-7 cells detected by real-time qRT-PCR, with GAPDH being used as a standardized internal control. All the data represented the relative fold changes in mRNA expression of the genes of interest ($N = 3$, mean ± SD, $^{*}P < 0.05$, $^{**}P < 0.01$ and $^{***}P < 0.001$, significantly different from the control; ns, not significantly different from the control). (**E**) and (**F**) Western blot to determine the translation of c-MYC, hTERT, Caspase3, Bax, γ-H2AX, 53BP1, and β-actin in MCF-7 cells treated with **2** (0–10 μM) and **3** (0–10 μM) respectively for 36 h ($N = 3$, mean ± SD, (*) $P < 0.05$, (**) $P < 0.01$ and (***) $P < 0.001$, significantly different from the control; ns, not significantly different from the control). (**G**) SA-β-gal assay was used to detect the effects of **2** (IC_{50} dose) and **3** (IC_{50} dose) on senescence of MCF-7 cells. (**H**) Comet assay analysis of DNA damage in MCF-7 cells after 36 h of treatment with **2** or **3** (10 μM). Compared with the control group, longer tails were observed in MCF-7 cells treated with **2** or **3**. (**I**) The effect of **2** and **3** on the concentration-dependent inhibition of telomerase activity. In the TRAP assay, MCF-7 cells were treated with the ligand **2** or **3** for 36 h.

Downloaded from https://academic.oup.com/nar/article/50/4/1829/6528910 by guest on 04 March 2022

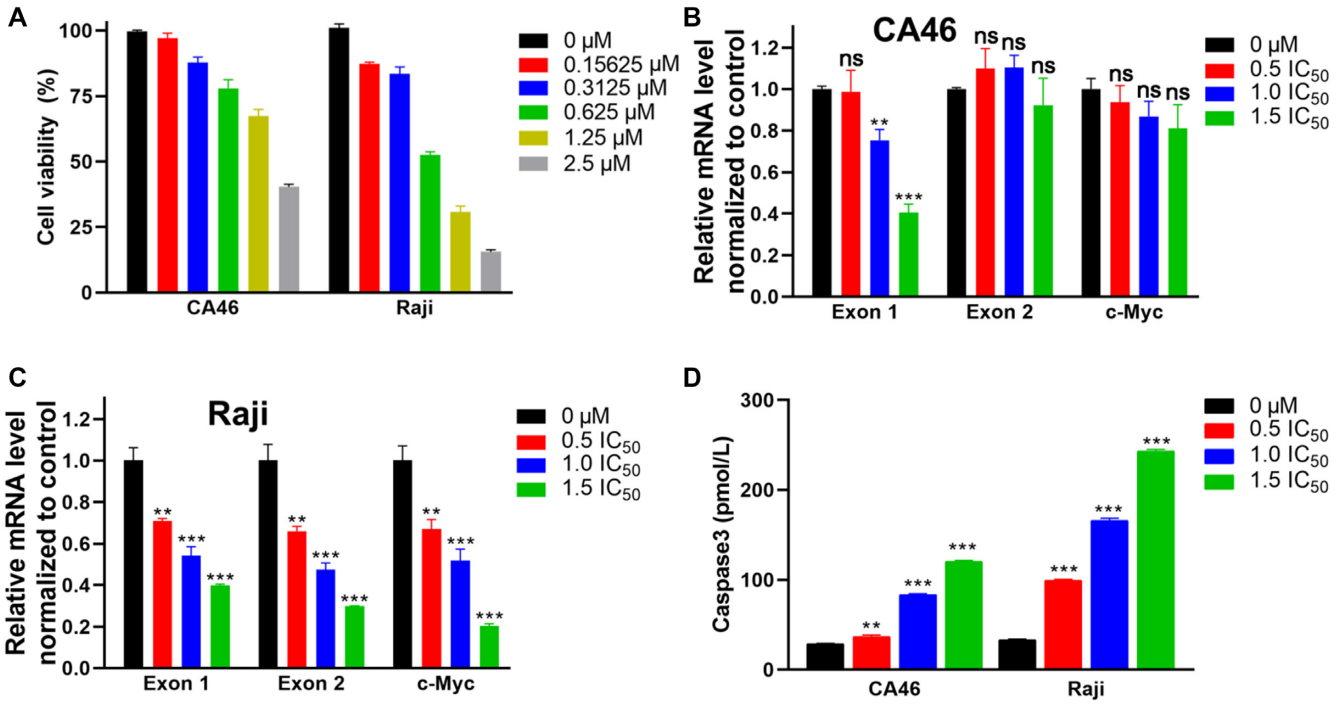

Figure 7. (**A**) CA46 and Raji cells treated with **3** (0–2.5 μM) for 36 h, respectively ($N = 3$, mean ± SD). (**B** and **C**) CA46 or Raji cells treated with **3** for 36 h, the mRNA expression of Exon1, Exon2 and c-MYC genes detected by real-time qRT-PCR, and GAPDH was used as a standardized internal control ($N = 3$, mean ± SD, $^{*}P < 0.05$, $^{**}P < 0.01$, and $^{***}P < 0.001$, significantly different from the control; ns, not significantly different from the control). (**D**) Effects of CA46 and Raji cells treated with **3** on caspase-3 protein in apoptosis pathway.

obviously inhibited by **2** or **3** (Figure 8C). Compared to the rapid growing tumors in the control group, the tumor growth found in group 1 (treated with **2**) was reduced by 41% while in group 2 (treated with **3**) it was reduced by 79% in terms of tumor weight (Figure 8D–F). In terms of the inhibitory effect of the ligands on tumor growth, the tumor tissues from the MCF-7 tumor-bearing nude mice treated with **2** (group 1) showed nuclear sequestration and fragmentation in H&E images compared to the control (group 0) (Figure 8G). More importantly, the tumor tissues from the mice treated with ligand **3** (group 2) showed more severe apoptosis and necrosis accompanied by notable nuclear fragmentation and nucleolysis. TUNEL staining data also showed that **3** promoted apoptosis of tumor cells to a greater extent than **2**. Furthermore, Ki67 staining assay clearly showed that **3** inhibited tumor cell proliferation more effectively than **2** (Figure 8G).

To further evaluate the biocompatibility and cytotoxicity *in vivo* of **2** and **3**, the mice were executed on the third day after the last injection of the ligands. The whole blood was collected for the assessment of various biochemical parameters including white blood cell count, lymphocyte count, neutrophil count, red blood cell count, hemoglobin, mean red blood cell volume, mean red blood cell hemoglobin content, mean red blood cell hemoglobin concentration, mean platelet volume, and platelet count. The results confirmed that no notable changes in these index values were observed between the treatment groups and control groups (Figure 9A). Moreover, the H&E staining sections of the main organs of the mice, the heart, liver, spleen, lung and kidney, were evaluated (Figure 9B). It was found that neither **2** nor **3** were toxic to these major organs. These results indicated that mice treated with the ligands did not exhibit inflammation or infection, suggesting that the ligands were highly histocompatible with normal tissues.

DISCUSSION

The DNA G4-structures of c-MYC promoter and telomere are known important drug targets for anticancer research (16). The discrimination of these two classes of G4-motif with ligands at the molecular level is a challenging task. Despite the fact that a number of G4 ligands have already been developed and that they show good selectivity toward G4-structures against double/single-stranded DNA and RNA molecules *in vitro*, how to design selective molecules to target the G4-structures of c-MYC promoter from telomere is rarely discussed in literature (27–35). In the present study, a new c-MYC G4–DNA structure-selective ligand that possesses two-directional multi-site interaction functionality and that is flexible to establish effective binding to the nucleotides of both flanking residues and loops of the G4-motif was developed. The sequence of the flanking residue and loop may define a unique binding site for recognition. The present study demonstrated, for the first time, the engineering of a non-selective molecular scaffold of thiazole orange that could be either telomeric- or c-MYC G4-selective through systematically regulating the functional groups in two directions to generate multi-site interaction ability. The interaction study using ^{1}H NMR titrations for the ligand and G4–DNA in solution suggested a π-stacking interaction mode at 5′-terminal or 3′-end of the G-tetrad. The in-

Downloaded from https://academic.oup.com/nar/article/50/4/1829/6528910 by guest on 04 March 2022

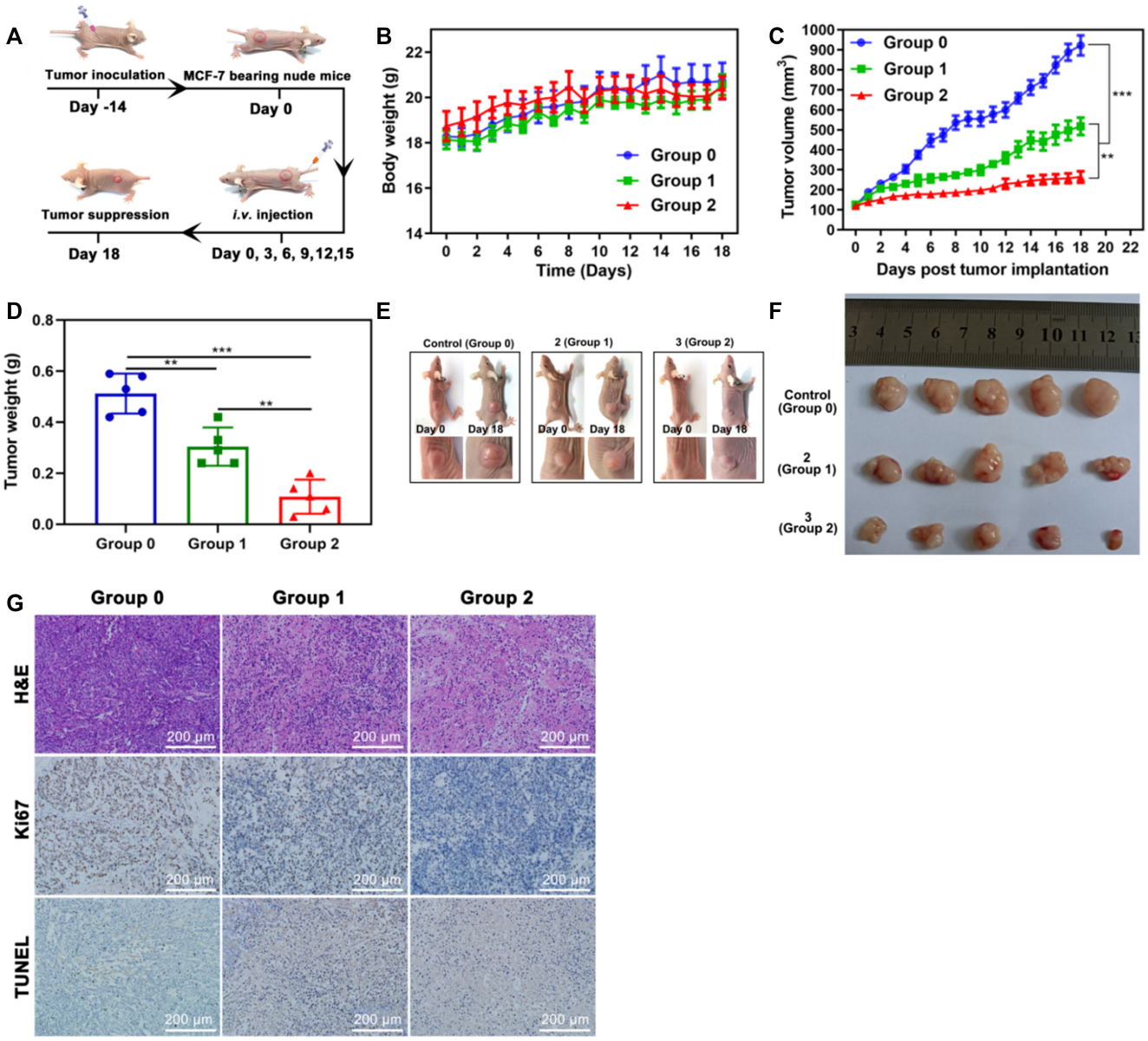

Figure 8. (**A**) A schematic diagram of *in vivo* treatment regimen of ligands **2** and **3** in MCF-7 tumor-bearing nude mice. (**B**) Body weight changes in MCF-7 tumor-bearing nude mice injected with ligand **2** or **3** (1.5 mg/kg) in tail vein over 18 days ($N = 5$, mean ± SD). (**C**) Time-dependent changes in tumor volume after different treatments for 18 days ($N = 5$, mean ± SD, $^{*}P < 0.05$, $^{**}P < 0.01$ and $^{***}P < 0.001$). (**D**) Weight of isolated tumors in MCF-7 tumor-bearing nude mice after 18 days of treatment ($N = 5$, mean ± SD, $^{*}P < 0.05$, $^{**}P < 0.01$ and $^{***}P < 0.001$). (**E**) Digital photographs of different groups of MCF-7 tumor-bearing nude mice on day 0 and day 18. (**F**) Digital photographs of isolated tumors from different groups of MCF-7-bearing nude mice after 18 days of treatment. (**G**) Representative histological images of H&E, TUNEL and Ki67 antigen immunofluorescence stained tumor tissue sections of MCF-7 tumor-bearing nude mice tumors from different groups after 18 days of treatment (scale bars is 200 μm).

creased ΔT_m of the ligand–G4 complex suggested that the ligand was able to bind to G4–DNA and thus stabilize the structure.

The ligand system designed based on a thiazole orange scaffold possesses a two-directional and multi-site interaction functionality. The structural modification derives two analogues selectively targeting G4-structures of telomere (ligand **2**) or c-MYC promoter (ligand **3**). Both ligands targeting G4-structures showed excellent live cell imaging performance. The intracellular co-localization studies with the G4-selective BG4 and BRACO19 consistently suggested that **3** was selectively binding to G4-structures. In addition, molecular modeling study suggested the involvement of the interaction **3**-G4 motif in the establishment of a special substituent group interaction with both the loop and flanking residues of c-MYC G4–DNA. Furthermore, in the study of inhibitory effects on telomerase activity in MCF-7 cells with **2** and **3**, it was found that **2** (telomeric G4-selective) showed better inhibitory ability than **3** (c-MYC G4-selective), which suggested that the two ligands probably had certain degrees of selectivity toward telomeric and c-MYC G4–DNA structures, respectively.

Downloaded from https://academic.oup.com/nar/article/50/4/1829/6528910 by guest on 04 March 2022

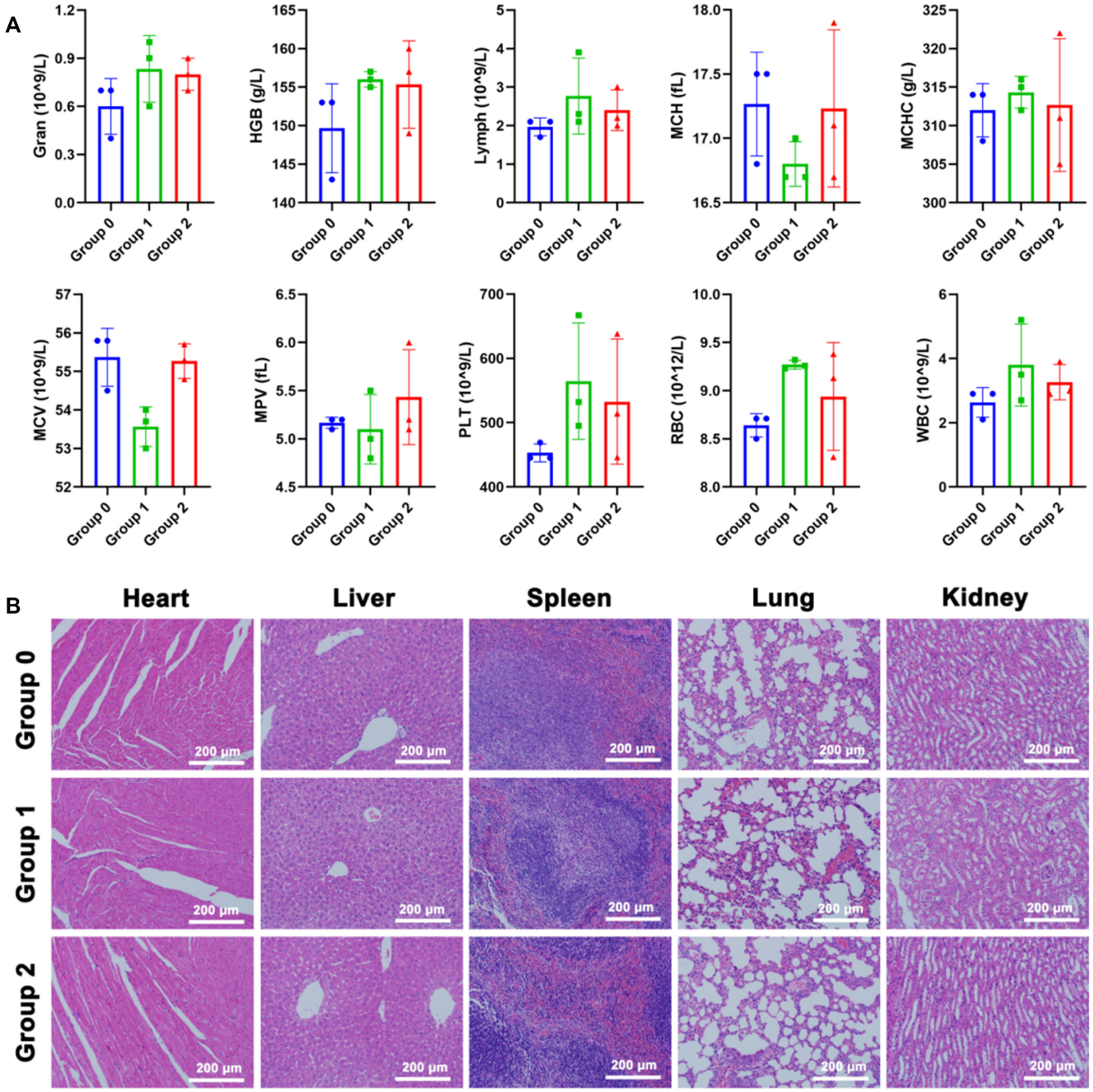

Figure 9. Effects on normal tissues and blood of nude mice after injection of ligand **2** or **3**. (**A**) Biochemical blood analysis of the ligands-treated mice 18 days post-injection under various conditions (group 0: treat with PBS, group 1: treat with ligand **2**, group 2: treat with ligand **3**) ($N = 3$, mean ± SD). (**B**) H&E-stained images of the major organs (heart, liver, spleen, lung and kidney) from different groups (scale bar is 200 μm).

Ligands **2** and **3** showed excellent cellular uptake efficiency in MCF-7 cells (Supplementary Figure S18). In the cytotoxicity evaluation by MTT assays, the IC_{50} values of the G4-selective ligands **2** and **3** against a panel of human cancer cells including U87, MCF-7, HeLa and PC3 were found to range from 4.2 to 6.6 μM, suggesting that the ligands had active anticancer activity. G4–DNA structures could possibly be the drug target of the ligands studied (11). In the cellular study, ligand **2** was more effective than **3** in the inhibition of telomerase activity probably due to its better selectivity toward telomere G4–DNA. Ligand **2** was found effectively shortened the telomere length in the TRAP assays in MCF-7 cells. The critically shortening of telomeres may not be able to maintain protective cap structures. Thus, the open telomeric ends may initiate DNA damage responses of the cancer cells. On the other hand, in the study of ligand effect on Exon-specific assays in CA46 cells (73,74), **3** showed remarkable suppression of Exon 1, Exon

Downloaded from https://academic.oup.com/nar/article/50/4/1829/6528910 by guest on 04 March 2022

2, and c-MYC in Raji cells while much less influence was observed for **2**. The results could indicate that **3** was a c-MYC G4-selective ligand.

In addition, both **2** and **3** were found to be able to downregulate c-MYC and hTERT gene expression in MCF-7 cells. The control gene CTCF, which was the repressive factor in the regulatory region of the hTERT promoter, was not affected by the ligands (Supplementary Figure S19). The repression of hTERT gene expression by the ligands may induce senescence of the cancer cells. As indicated from the SA-β-gal assays (Figure 6G), **2** and **3** at IC_{50} concentration were able to induce remarkable cellular senescence of MCF-7 cancer cells. This was most likely to be attributed to the effect of the ligands that markedly suppressed MYC expression (75). It thus results in proliferative arrest of the cancer cells (76). Furthermore, the ligands were found to be able to upregulate γ-H2AX and 53BP1 markedly in MCF-7 cancer cells, which indicated that DNA damage in the cells was induced by **2** and **3**. This is probably a consequent of the persistent inhibition of hTERT gene expression by the ligand. The comet assays (Figure 6H) also provide the evidence of DNA damage in the cancer cells after treated with the ligands. The induced DNA damage responses in MCF-7 cells may cause the transition of cells into a state of senescence. The accumulating DNA damage in MCF-7 cells may eventually cause substantial cell death (77,78).

The investigation of *in vivo* antitumor activity of ligands **2** and **3** in MCF-7 tumor-bearing mice revealed that **3**, which was selective to c-MYC promoter G4–DNA, was able to inhibit tumor growth remarkably (79% tumor weight reduction). The antitumor activity of **3** was better than that of **2** (41% tumor weight reduction). The concentration of ligands in the bloodstream of the mice after intravenous administrations was investigated with HPLC-MS. The ligand concentration in blood over time was found to have decreased gradually (Supplementary Figure S25). In general, the ability of **3** to be retained in the bloodstream was better than that of **2**. The results showed that there were about 56% of **3** remaining in the bloodstream while there were only 40% of **2** after injection for 2 h. One of the possible factors for ligand **3** showing better antitumor activity could be the ligand possessing better *in vivo* stability. Nonetheless, both ligands were eliminated from the bloodstream after 24 h. Moreover, the evaluation of *in vivo* biocompatibility and cytotoxicity also showed that neither ligands **2** and **3** were toxic to the major organs including the heart, liver, spleen, lung, and kidney, and neither of them had caused any inflammation or infection, suggesting that the ligands were highly histocompatible with normal tissues. Taken together, the results may provide insights into the designing of anticancer drugs targeting the c-MYC G4-structures with high selectivity and thus the off-target effects could be possibly reduced.

DATA AVAILABILITY

The datasets generated and/or analyzed during the current study are available from the corresponding author on reasonable request.

SUPPLEMENTARY DATA

Supplementary Data are available at NAR Online.

ACKNOWLEDGEMENTS

We acknowledge Dr Shan-Yue Guan (Instrumental Analysis & Research Center, Sun Yat-Sen University), Dr Zhi-Shu Huang and Dr Shuo-Bin Chen (School of Pharmaceutical Sciences, Sun Yat-Sen University) for their assistance on the NMR experiments for the interaction study.

FUNDING

National Natural Science Foundation of China [81473082, 22077020, 32050410289]; Natural Science Foundation of Guangdong Province, China [2017A030313078, 2017A030313071, 2019A1515011799]; Jiangmen Program for Innovative Research Team [201863010018019806], Department of Education of Guangdong Province, China [2016KCXTD005, 2017KSYS010]; Department of Agriculture and Rural Affairs of Guangdong Province, China [2018LM2175]; Health and Medical Research Fund (HMRF) of the Food and Health Bureau, Hong Kong SAR [19200231]; PolyU Startup Fund [P0035712]. Funding for open access charge: Natural Science Foundation of Guangdong Province, China [2019A1515011799].

Conflict of interest statement. The authors declare no conflicts of interest.

REFERENCES

1. Bochman,M.L., Paeschke,K. and Zakian,V.A. (2012) DNA secondary structures: stability and function of G-quadruplex structures. *Nat. Rev. Genet.*, **13**, 770–780.
2. Yanaihara,N. and Harris,C.C. (2013) MicroRNA involvement in human cancers. *Clin. Chem.*, **59**, 1811–1812.
3. Diolaiti,M.E., Cimini,B.A., Kageyama,R., Charles,F.A. and Stohr,B.A. (2013) In situ visualization of telomere elongation patterns in human cells. *Nucleic Acids Res.*, **41**, 492–503.
4. Byrd,A.K. and Raney,K.D. (2017) Structure and function of Pif1 helicase. *Biochem. Soc. T.*, **45**, 1159–1171.
5. Valton,A.-L., Hassan-Zadeh,V., Lema,I., Boggetto,N., Alberti,P., Saintome,C., Riou,J.-F. and Prioleau,M.-N. (2014) G4 motifs affect origin positioning and efficiency in two vertebrate replicators. *Embo J.*, **33**, 732–746.
6. Cui,Y., Koirala,D., Kang,H., Dhakal,S., Yangyuoru,P., Hurley,L.H. and Mao,H. (2014) Molecular population dynamics of DNA structures in a bcl-2 promoter sequence is regulated by small molecules and the transcription factor hnRNP LL. *Nucleic Acids Res.*, **42**, 5755–5764.
7. Ge,L., Sun,X., Hong,Q. and Li,F. (2017) Ratiometric nanocluster beacon: a label-free and sensitive fluorescent DNA detection platform. *ACS Appl. Mater. Interfaces*, **9**, 13102–13110.
8. Lam,E.Y.N., Beraldi,D., Tannahill,D. and Balasubramanian,S. (2013) G-quadruplex structures are stable and detectable in human genomic DNA. *Nat. Commun.*, **4**, 1796–1796.
9. Elisa Bergues-Pupo,A., Ricardo Arias-Gonzalez,J., Carmen Moron,M., Fiasconaro,A. and Falo,F. (2015) Role of the central cations in the mechanical unfolding of DNA and RNA G-quadruplexes. *Nucleic Acids Res.*, **43**, 7638–7647.
10. Sahakyan,A.B., Chambers,V.S., Marsico,G., Santner,T., Di Antonio,M. and Balasubramanian,S. (2017) Machine learning model for sequence-driven DNA G-quadruplex formation. *Sci. Rep.*, **7**, 14535–14535.
11. Balasubramanian,S., Hurley,L.H. and Neidle,S. (2011) Targeting G-quadruplexes in gene promoters: a novel anticancer strategy?*Nat. Rev. Drug Disco.*, **10**, 261–275.

Downloaded from https://academic.oup.com/nar/article/50/4/1829/6528910 by guest on 04 March 2022

12. Dickerhoff,J., Dai,J. and Yang,D. (2021) Structural recognition of the MYC promoter G-quadruplex by a quinoline derivative: insights into molecular targeting of parallel G-quadruplexes. *Nucleic Acids Res.*, **49**, 5905–5915.
13. Spiegel,J., Adhikari,S. and Balasubramanian,S. (2020) The structure and function of DNA G-quadruplexes. *Trends Chem.*, **2**, 123–136.
14. Kwok,C.K. and Merrick,C.J. (2017) G-Quadruplexes: prediction, characterization, and biological application. *Trends. Biotechnol.*, **35**, 997–1013.
15. Chambers,V.S., Marsico,G., Boutell,J.M., Di Antonio,M., Smith,G.P. and Balasubramanian,S. (2015) High-throughput sequencing of DNA G-quadruplex structures in the human genome. *Nat. Biotechnol.*, **33**, 877–881.
16. Neidle,S. (2016) Quadruplex nucleic acids as novel therapeutic targets. *J. Med. Chem.*, **59**, 5987–6011.
17. Mollaoglu,G., Guthrie,M.R., Boehm,S., Braegelmann,J., Can,I., Ballieu,P.M., Marx,A., George,J., Heinen,C., Chalishazar,M.D. *et al.* (2017) MYC drives progression of small cell lung cancer to a variant neuroendocrine subtype with vulnerability to aurora kinase inhibition. *Cancer Cell*, **31**, 270–285.
18. Kaiser,C.E., Van Ert,N.A., Agrawal,P., Chawla,R., Yang,D. and Hurley,L.H. (2017) Insight into the complexity of the i-motif and G-quadruplex DNA structures formed in the KRAS promoter and subsequent drug induced gene repression. *J. Am. Chem. Soc.*, **139**, 8522–8536.
19. Rodriguez,J., Mosquera,J., Couceiro,J.R., Vazquez,M.E. and Mascarenas,J.L. (2016) Ruthenation of non-stacked guanines in DNA G-quadruplex structures: enhancement of c-MYC expression. *Angew. Chem. Int. Edit.*, **55**, 15615–15618.
20. Dang,C.V. (2012) MYC on the path to cancer. *Cell*, **149**, 22–35.
21. Chen,B.-J., Wu,Y.-L., Tanaka,Y. and Zhang,W. (2014) Small molecules targeting c-Myc oncogene: promising anti-cancer therapeutics. *Int. J. Biol. Sci.*, **10**, 1084–1096.
22. Li,Z., Liu,C., Huang,C., Meng,X., Zhang,L., He,J. and Li,J. (2016) Quinazoline derivative QPB-15e stabilizes the c-myc promoter G-quadruplex and inhibits tumor growth in vivo. *Oncotarget*, **7**, 34266–34276.
23. Yang,H., Zhong,H.-J., Leung,K.-H., Chan,D.S.-H, Ma,V.P.-Y, Fu,W.-C, Nanjunda,R, Wilson,W.D, Ma,D.-L and Leung,C.-H. (2013) Structure-based design of flavone derivatives as c-myc oncogene down-regulators. *Eur. J. Pharm. Sci.*, **48**, 130–141.
24. Tawani,A., Mishra,S.K. and Kumar,A. (2017) Structural insight for the recognition of G-quadruplex structure at human c-myc promoter sequence by flavonoid Quercetin. *Sci. Rep.*, **7**, 3600–3600.
25. Siddiqui-Jain,A., Grand,C.L., Bearss,D.J. and Hurley,L.H. (2002) Direct evidence for a G-quadruplex in a promoter region and its targeting with a small molecule to repress c-MYC transcription. *Proc. Natl. Acad. Sci. U.S A.*, **99**, 11593–11598.
26. Grand,C.L., Han,H.Y., Munoz,R.M., Weitman,S., Von Hoff,D.D., Hurley,L.H. and Bearss,D.J. (2002) The cationic porphyrin TMPyP4 down-regulates c-MYC and human telomerase reverse transcriptase expression and inhibits tumor growth in vivo. *Mol. Cancer Ther.*, **1**, 565–573.
27. Che,T., Chen,S.-B., Tu,J.-L., Wang,B., Wang,Y.-Q., Zhang,Y., Wang,J., Wang,Z.-Q., Zhang,Z.-P., Ou,T.-M. *et al.* (2018) Discovery of novel Schizocommunin derivatives as telomeric G-quadruplex ligands that trigger telomere dysfunction and the deoxyribonucleic acid (DNA) damage response. *J. Med. Chem.*, **61**, 3436–3453.
28. Micco,M., Collie,G.W., Dale,A.G., Ohnmacht,S.A., Pazitna,I., Gunaratnam,M., Reszka,A.P. and Neidle,S. (2013) Structure-based design and evaluation of naphthalene diimide G-quadruplex ligands as telomere targeting agents in pancreatic cancer cells. *J. Med. Chem.*, **56**, 2959–2974.
29. Lombardo,C.M., Martinez,I.S., Haider,S., Gabelica,V., De Pauw,E., Moses,J.E. and Neidle,S. (2010) Structure-based design of selective high-affinity telomeric quadruplex-binding ligands. *Chem. Commun.*, **46**, 9116–9118.
30. Long,W., Zheng,B.-X., Huang,X.-H., She,M.-T., Liu,A.-L., Zhang,K., Wong,W.-L. and Lu,Y.-J. (2021) Molecular recognition and imaging of human telomeric G-quadruplex DNA in live cells: a systematic advancement of thiazole orange scaffold to enhance binding specificity and inhibition of gene expression. *J. Med. Chem.*, **64**, 2125–2138.
31. Kumar,R., Chand,K., Bhowmik,S., Das,R.N., Bhattacharjee,S., Hedenstrom,M. and Chorell,E. (2020) Subtle structural alterations in G-quadruplex DNA regulate site specificity of fluorescence light-up probes. *Nucleic Acids Res.*, **48**, 1108–1119.
32. Zhai,Q., Gao,C., Ding,J., Zhang,Y., Islam,B., Lan,W., Hou,H., Deng,H., Li,J., Hu,Z. *et al.* (2019) Selective recognition of c-MYC Pu22 G-quadruplex by a fluorescent probe. *Nucleic Acids Res.*, **47**, 2190–2204.
33. Hu,M.-H., Wang,Y.-Q., Yu,Z.-Y., Hu,L.-N., Ou,T.-M., Chen,S.-B., Huang,Z.-S. and Tan,J.-H. (2018) Discovery of a new four-leaf clover-like ligand as a potent c-MYC transcription inhibitor specifically targeting the promoter G-quadruplex. *J. Med. Chem.*, **61**, 2447–2459.
34. Wang,K.-B., Elsayed,M.S.A., Wu,G., Deng,N., Cushman,M. and Yang,D. (2019) Indenoisoquinoline topoisomerase inhibitors strongly bind and stabilize the MYC promoter G-quadruplex and downregulate MYC. *J. Am. Chem. Soc.*, **141**, 11059–11070.
35. Panda,D., Debnath,M., Mandal,S., Bessi,I., Schwalbe,H. and Dash,J. (2015) A nucleus-imaging probe that selectively stabilizes a minor conformation of c-MYC G-quadruplex and down-regulates c-MYC transcription in human cancer cells. *Sci. Rep.*, **5**. 13183–13183.
36. Hu,M.-H., Zhou,J., Luo,W.-H., Chen,S.-B., Huang,Z.-S., Wu,R. and Tan,J.-H. (2019) Development of a smart fluorescent sensor that specifically recognizes the c-MYC G-quadruplex. *Anal. Chem.*, **91**, 2480–2487.
37. Carvalho,J., Quintela,T., Gueddouda,N.M., Bourdoncle,A., Mergny,J.-L., Salgado,G.F., Queiroz,J.A. and Cruz,C. (2018) Phenanthroline polyazamacrocycles as G-quadruplex DNA binders. *Org. Biomol. Chem.*, **16**, 2776–2786.
38. Zheng,B.-X., Long,W., Zhang,Y.-H., Huang,X.-H., Chen,C.-C., Zhong,D.-X., She,M.-T., Chen,Z.-X., Cai,D.-P., Lu,Y.-J. *et al.* (2020) Rational design of red fluorescent and selective G-quadruplex DNA sensing probes: The study of interaction signaling and the molecular structural relationship achieving high specificity. *Sensors Actuat. B-Chem.*, **314**, 128075.
39. Zheng,B.-X., She,M.-T., Long,W., Xu,Y.-Y., Zhang,Y.-H., Huang,X.-H., Liu,W., Hou,J.-Q., Wong,W.-L. and Lu,Y.-J. (2020) A small-sized benzothiazole-indolium fluorescent probe: the study of interaction specificity targeting c-MYC promoter G-quadruplex structures and live cell imaging. *Chem. Commun.*, **56**, 15016–15019.
40. Vorlickova,M., Kejnovska,I., Bednarova,K., Renciuk,D. and Kypr,J. (2012) Circular dichroism spectroscopy of DNA: from duplexes to quadruplexes. *Chirality*, **24**, 691–698.
41. Kypr,J., Kejnovska,I., Renciuk,D. and Vorlickova,M. (2009) Circular dichroism and conformational polymorphism of DNA. *Nucleic Acids Res.*, **37**, 1713–1725.
42. Bishop,G.R. and Chaires,G.B. (2002) Characterization of DNA structures by circular dichroism. *Curr. Protoc. Nucleic Acid Chem.*, **11**, 7.11.1–7.11.8.
43. Long,W., Lu,Y.-J., Zhang,K., Huang,X.-H., Hou,J.-Q., Cai,S.-Y., Li,Y., Du,X., Luyt,L.G., Wong,W.-L. *et al.* (2018) Boosting the turn-on fluorescent signaling ability of thiazole orange dyes: the effectiveness of structural modification site and its unusual interaction behavior with nucleic acids. *Dyes Pigment.*, **159**, 449–456.
44. Bala,I., Bhardwaj,V., Hariharan,S. and Kumar,M. (2006) Analytical methods for assay of ellagic acid and its solubility studies. *J. Pharmaceut. Biomed. Anal.*, **40**, 206–210.
45. Stootman,F.H., Fisher,D.M., Rodger,A. and Aldrich-Wright,J.R. (2006) Improved curve fitting procedures to determine equilibrium binding constants. *Analyst*, **131**, 1145–1151.
46. Xie,X., Choi,B., Largy,E., Guillot,R., Granzhan,A. and Teulade-Fichou,M.-P. (2013) Asymmetric distyrylpyridinium dyes as red-emitting fluorescent probes for quadruplex DNA. *Chem.-Eur. J.*, **19**, 1214–1226.
47. Yvon,H.J., (2012) In: *A Guide to Recording Fluorescence Quantum Yields*. HORIBA: Jobin Yvon Ltd, Stanmore, Middlesex, UK.
48. Brouwer,A.M. (2011) Standards for photoluminescence quantum yield measurements in solution (IUPAC technical report). *Pure. Appl. Chem.*, **83**, 2213–2228.
49. Morris,G.M., Huey,R., Lindstrom,W., Sanner,M.F., Belew,R.K., Goodsell,D.S. and Olson,A.J. (2009) AutoDock4 and autodocktools4: automated docking with selective receptor flexibility. *J. Comput. Chem.*, **30**, 2785–2791.

Downloaded from https://academic.oup.com/nar/article/50/4/1829/6528910 by guest on 04 March 2022

50. Forli,S., Huey,R., Pique,M.E., Sanner,M.F., Goodsell,D.S. and Olson,A.J. (2016) Computational protein-ligand docking and virtual drug screening with the Autodock suite. *Nat. Protoc.*, **11**, 905–919.
51. Kim,N.W. and Wu,F. (1997) Advances in quantification and characterization of telomerase activity by the telomeric repeat amplification protocol (TRAP). *Nucleic Acids Res.*, **25**, 2595–2597.
52. Kohler,O., Venkatrao,D., Jarikote,D.V. and Seitz,O. (2005) Forced intercalation probes (FIT probes): thiazole orange as a fluorescent base in peptide nucleic acids for homogeneous single-nucleotide-polymorphism detection. *Chembiochem*, **6**, 69–77.
53. Yan,J.-W., Ye,W.-J., Chen,S.-B., Wu,W.-B., Hou,J.-Q., Ou,T.-M., Tan,J.-H., Li,D., Cu,L.-Q. and Huang,Z.-S. (2012) Development of a universal colorimetric indicator for G-quadruplex structures by the fusion of thiazole orange and isaindigotone skeleton. *Anal. Chem.*, **84**, 6288–6292.
54. Lu,Y.-J., Deng,Q., Hou,J.-Q., Hu,D.-P., Wang,Z.-Y., Zhang,K., Luyt,L.G., Wong,W.-L. and Chow,C.-F. (2016) Molecular engineering of thiazole orange dye: change of fluorescent signaling from universal to specific upon binding with nucleic acids in bioassay. *ACS Chem. Biol.*, **11**, 1019–1029.
55. Dai,J., Carver,M., Hurley,L.H. and Yang,D. (2011) Solution structure of a 2:1 quindoline-c-MYC G-quadruplex: insights into G-quadruplex-interactive small molecule drug design. *J. Am. Chem. Soc.*, **133**, 17673–17680.
56. Chen,Y. and Yang,D. (2012) Sequence, stability, and structure of G-quadruplexes and their interactions with drugs. *Curr. Protoc. Nucleic Acid Chem.*, **Chapter 17**, Unit17.5.
57. Feigon,J., Koshlap,K.M. and Smith,F.W. (1995) 1H NMR spectroscopy of DNA triplexes and quadruplexes. *Method. Enzymol.*, **261**, 225–255.
58. Phan,A.T., Kuryavyi,V., Gaw,H.Y. and Patel,D.J. (2005) Small-molecule interaction with a five-guanine-tract G-quadruplex structure from the human MYC promoter. *Nat. Chem. Biol.*, **1**, 167–173.
59. Ambrus,A., Chen,D., Dai,J.X., Jones,R.A. and Yang,D.Z. (2005) Solution structure of the biologically relevant G-quadruplex element in the human c-MYC promoter. Implications for G-quadruplex stabilization. *Biochemistry*, **44**, 2048–2058.
60. Huang,Z.-L., Dai,J., Luo,W.-H., Wang,X.-G., Tan,J.-H., Chen,S.-B. and Huang,Z.-S. (2018) Identification of G-quadruplex-binding protein from the exploration of RGG motif/G-quadruplex interactions. *J. Am. Chem. Soc.*, **140**, 17945–17955.
61. Chung,W.J., Heddi,B., Hamon,F., Teulade-Fichou,M.-P. and Anh Tuan,P. (2014) Solution structure of a G-quadruplex bound to the bisquinolinium compound Phen-DC3. *Angew. Chem. Int. Ed.*, **53**, 999–1002.
62. Biffi,G., Tannahill,D., McCafferty,J. and Balasubramanian,S. (2013) Quantitative visualization of DNA G-quadruplex structures in human cells. *Nat. Chem.*, **5**, 182–186.
63. Artusi,S., Perrone,R., Lago,S., Raffa,P., Di Iorio,E., Palu,G. and Richter,S.N. (2016) Visualization of DNA G-quadruplexes in herpes simplex virus 1-infected cells. *Nucleic Acids Res.*, **44**, 10343–10353.
64. Liu,H.-Y., Zhao,Q., Zhang,T.-P., Wu,Y., Xiong,Y.-X., Wang,S.-K., Ge,Y.-L., He,J.-H., Lv,P., Ou,T.-M. *et al.* (2016) Conformation selective antibody enables genome profiling and leads to discovery of parallel G-quadruplex in human telomeres. *Cell. Chem. Biol.*, **23**, 1261–1270.
65. Shay,J.W. (2016) Role of telomeres and telomerase in aging and cancer. *Cancer Discov.*, **6**, 584–593.
66. Qin,Q.P., Meng,T., Tan,M.X., Liu,Y.C., Luo,X.J., Zou,B.Q. and Liang,H. (2018) Synthesis, crystal structure and biological evaluation of a new dasatinib copper(II) complex as telomerase inhibitor. *Eur. J. Med. Chem.*, **143**, 1597–1603.
67. Zhao,Y., Cheng,D., Wang,S. and Zhu,J. (2014) Dual roles of c-Myc in the regulation of hTERT gene. *Nucleic Acids Res.*, **42**, 10385–10398.
68. Wang,S.-T., Huang,S.-W., Liu,K.-T., Lee,T.-Y., Shieh,J.-J. and Wu,C.-Y. (2020) Atorvastatin-induced senescence of hepatocellular carcinoma is mediated by downregulation of hTERT through the suppression of the IL-6/STAT3 pathway. *Cell Death Discov.*, **6**, 17.
69. Gu,J., Kagawa,S., Takakura,M., Kyo,S., Inoue,M., Roth,J.A. and Fang,B.L. (2000) Tumor-specific transgene expression from the human telomerase reverse transcriptase promoter enables targeting of the therapeutic effects of the Bax gene to cancers. *Cancer Res.*, **60**, 5359–5364.
70. Mantena,S.K., Sharma,S.D. and Katiyar,S.K. (2006) Berberine, a natural product, induces G(1)-phase cell cycle arrest and caspase-3-dependent apoptosis in human prostate carcinoma cells. *Mol. Cancer Ther.*, **5**, 296–308.
71. Turinetto,V. and Giachino,C. (2015) Multiple facets of histone variant H2AX: a DNA double-strand-break marker with several biological functions. *Nucleic Acids Res.*, **43**, 2489–2498.
72. Michelini,F., Pitchiaya,S., Vitelli,V., Sharma,S., Gioia,U., Pessina,F., Cabrini,M., Wang,Y.J., Capozzo,I., Iannelli,F. *et al.* (2017) Damage-induced lncRNAs control the DNA damage response through interaction with DDRNAs at individual double-strand breaks. *Nat. Cell Biol.*, **19**, 1400–1411.
73. Brown,R.V., Danford,F.L., Gokhale,V., Hurley,L.H. and Brooks,T.A. (2011) Demonstration that drug-targeted down-regulation of MYC in non-Hodgkins lymphoma is directly mediated through the promoter G-quadruplex. *J. Biol. Chem.*, **286**, 41018–41027.
74. Boddupally,P.V.L., Hahn,S., Beman,C., De,B., Brooks,T.A., Gokhale,V. and Hurley,L.H. (2012) Anticancer activity and cellular repression of c-MYC by the G-quadruplex-stabilizing 11-piperazinylquindoline is not dependent on direct targeting of the G-quadruplex in the c-MYC promoter. *J. Med. Chem.*, **55**, 6076–6086.
75. Wu,C-H., van Riggelen,J., Yetil,A., Fan,A.C., Bachireddy,P. and Felsher,D.W. (2007) Cellular senescence is an important mechanism of tumor regression upon c-Myc inactivation. *Proc. Nati. Acad. Sci. U.S.A.*, **104**, 13028–13033.
76. Patel,P.L., Suram,A., Mirani,N., Bischof,O. and Herbig,U. (2016) Derepression of hTERT gene expression promotes escape from oncogene-induced cellular senescence. *Proc. Nati. Acad. Sci. U.S.A.*, **113**, E5024–E5033.
77. De Magis,A., Manzo,S.G., Russo,M., Marinello,J., Morigi,R., Sordet,O. and Capranico,G. (2019) DNA damage and genome instability by G-quadruplex ligands are mediated by R loops in human cancer cells. *Proc. Nati. Acad. Sci. U.S.A.*, **116**, 816–825.
78. Song,J.H., Kang,H.-J., Luevano,L.A., Gokhale,V., Wu,K., Pandey,R., Chow,H.H.S., Hurley,L.H. and Kraft,A.S. (2019) Small-molecule-targeting hairpin loop of hTERT promoter G-quadruplex induces cancer cell death. *Cell Chem. Biol.*, **26**, 1110–1121.

Downloaded from https://academic.oup.com/nar/article/50/4/1829/6528910 by guest on 04 March 2022